

Creep Fatigue Crack Growth and Creep Crack Growth Behavior of P92 at Elevated Temperature

A Thesis

Presented in Partial Fulfillment of the Requirements for the

Degree of Master of Science

with a

Major in Mechanical Engineering

in the

College of Graduate Studies

University of Idaho

by

Anthony E. DeSantis

Approved by:

Major Professor: Robert Stephens, Ph.D., P.E.

Committee Members: Michael Maughan, Ph.D., P.E.; Gabriel Potirniche, Ph.D., P.E.

Department Chair: Gabriel Potirniche, Ph.D., P.E.

December 2022

ABSTRACT

High chromium heat resistant steels are commonly used for boiler components that are operated around 600°C in ultra-supercritical (USC) thermal power plants. This study focuses on the creep fatigue crack growth, creep crack growth and creep brittle or ductile behavior of ASME P92 steel at 650°C. All specimens were machined from a header pipe in a homogeneous fashion. A side groove analysis was performed to determine the best side groove percentage to use for a uniform crack front propagation which found a 10% total side groove to be the best percentage. The study showed that for creep fatigue crack growth tests the contour integral $(C_t)_{avg}$ correlated the three tests with hold times of 60 s better than the stress intensity factor K. The creep crack growth tests showed similar results with the contour integral C^* being a better crack tip parameter to characterize the data rather than the stress intensity factor K. The creep crack growth tests behaved in a creep ductile manner according to the load line displacement ratio and the non-dimensional crack velocity analyses.

ACKNOWLEDGEMENTS

Thank you to EPRI for sponsoring this research, providing test specimens, and helping with test analysis. Specifically, John Seifert from EPRI and Ian Perrin, a private consultant, for all your help with analyzing tests.

Thank you to Kaitlin Tabaracci, Beck Kanaskie and most of all Dr. Robert Stephens for helping me out through the writing process of this thesis. I could not have accomplished everything without all their help and support.

Thank you to Dr. Robert Stephens for guiding me through graduate school. You made the process seamless and fun. Not many professors work hands on with students in the lab and I will always remember the late-night brainstorming and test set ups. Thank you for becoming a part of my life this past year and a half, I appreciate everything you have done for me!

Thank you to my lab colleagues Troy Hanes, Zane Holliday, and Michael Myers for helping me out in the lab over the past year and a half. It has been a pleasure working with you all!

Thank you to Cody Gibson for teaching me everything I know about the MATEL lab and equipment. You made it possible for this research to be completed. I once told you that I try to surround myself with better people to help myself grow as a person and that you are one of those people. I still stand by that, and I hope southern Idaho is treating you well.

Thank you to Kaitlin Tabaracci for spending countless hours in the lab, library, office, and machine shop. I know you are going to accomplish amazing things. I will now give you the honor of keeping our single shared braincell for the rest of your college career. I don't think you'll need it, but it can't hurt.

DEDICATIONS

To my parents, I would not be the scholar, leader, athlete, or gentleman I am today without your push to succeed in all ways of life. Who knows where the future will take me, but I know one thing without a doubt is that it is all thanks to you two. I love you both and thank you for your unconditional support!

To my sister, I didn't really talk to you for a while because of how immature you were. I have watched you grow as a person so much in the last few years and I am glad that we have become closer over the years. Do what makes you happy and have fun while doing it!

To Katelyn, you supported me through the tough times of college by my side and from 2500 miles away. Our love is not faded by the distance. You have stuck with me through thick and thin and I hope your career goals will eventually lead you back to me. I love you!

TABLE OF CONTENTS

ABSTRACT	II
ACKNOWLEDGEMENTS	III
DEDICATIONS	IV
TABLE OF CONTENTS	V
LIST OF FIGURES	VII
LIST OF TABLES	IX
NOMENCLATURE	X
1. INTRODUCTION	1
2. LITERATURE REVIEW	3
2.1 FRACTURE MECHANICS	3
2.2 CREEP.....	4
2.3 CREEP CRACK GROWTH PARAMETERS	8
3. EXPERIMENTAL DETAILS	12
3.1 MATERIAL AND SPECIMEN GEOMETRY	12
3.2 EXPERIMENTAL TESTING EQUIPMENT	13
3.3 TESTING PROCEDURES.....	16
4. RESULTS AND DISCUSSION	19
4.1 TESTING MATRIX	19
4.2 DCPD VS CRACK LENGTH	20
4.3 P92 CFCG.....	22
4.4 P92 CCG.....	24
4.6 FRACTOGRAPHY	30
4.6.1 EDS.....	31
4.6.2 Creep Voids and Secondary Cracking.....	32
4.6.3 Specimen 8 Void Density Analysis.....	35

5. CONCLUSIONS AND RECOMMENDATIONS	39
5.1 CONCLUSIONS	39
5.2 RECOMMENDATIONS	40
6. REFERENCES.....	42
7. APPENDICIES	44
APPENDIX A. RAW TEST DATA	44
APPENDIX B. LOAD SHEDDING.....	53
APPENDIX C. VOID DENSITY ANALYSIS.....	54

LIST OF FIGURES

Fig. 1.1. Example of a boiler header pipe. [10]	2
Fig. 2.1. Three modes of loading. [2]	3
Fig. 2.2. Deformation mechanisms at different stresses and temperatures. [4]	5
Fig. 2.3. Creep mechanisms. [7]	6
Fig. 2.4. Schematic representation of the levels of creep deformation under which creep crack growth can occur. Small Scale Creep (a), Transition Creep (b), Extensive Creep (c). Adapted from [1]	7
Fig. 2.5. Comparison of crack length Δa vs t/t_f between Cr-Mo-V steel and IN 100. 1 and 2 correspond to uniform velocity portion and accelerating portion, respectively; t_f = creep fracture life. [8]	10
Fig. 2.6. Comparison of load-line displacement of the weldment and base metal. [9].....	11
Fig. 3.1. Specimen geometry.	13
Fig. 3.2. Load frames from left to right: MTS 312.11 44 kN (10 kip), MTS 312.12 97 kN (22 kip), deadweight creep frame.....	14
Fig. 3.3. DCPD spot welding locations.....	15
Fig. 3.4. Extensometer knife edge placement.	16
Fig. 3.5. Test waveforms.....	17
Fig. 4.1. Fracture surfaces of all nine specimens.....	19
Fig. 4.2. Crack front for three different side groove percentages.	20
Fig. 4.3. Normalized DCPD vs crack length plot.	21
Fig. 4.4. CFCG plots from left (a) da/dN vs ΔK and the right (b) da/dt vs K_{max}	23
Fig. 4.5. Crack growth rate, da/dt , versus contour integral, $(C_t)_{avg}$	24
Fig. 4.6. (a) Graph of 10% and no side groove CCG specimens, (b) graph of just 10% side grooved CCG specimens.....	25
Fig. 4.7. Crack growth rate, da/dt , versus contour integral, C^*	26
Fig. 4.8. Comparing Tabuchi et al. [9] round robin data with tests performed.	27
Fig. 4.9. (a) Load line displacement for 10% side grooved CCG tests. (b) Load line displacement breakdown for specimen 6.....	28
Fig. 4.10. (a) EDS spot used for material composition, (b) EDS spot used for oxidation layer.	31

Fig. 4.11. (a) EDS material reading for Fig. 4.10(a), (b) EDS material reading for Fig. 4.10(b).....	31
Fig. 4.12. Points EDS was used to see BN inclusions.	32
Fig. 4.13. EDS material reading for BN spots in Fig. 4.12.....	32
Fig. 4.14. (a) Specimen 6, (b) Specimen 7, (c) Specimen 8.	33
Fig. 4.15. Specimen 6, 7, and 8 fracture surface.....	34
Fig. 4.16. Example of secondary cracking seen below the fracture surface.	35
Fig. 4.17. Image from EPRI of where each plane was sectioned. [10].....	35
Fig. 4.18. Optical images of each plane of specimen 8 with points marked where void density analyses was conducted.	36
Fig. 4.19. Left three graphs are comparing a specific distance below the fracture surface per graph for each plane. Right three graphs are comparing each plane per graph at different distances below the crack front.	38

LIST OF TABLES

Tab. 3.1. Material composition from EPRI. [10]	12
Tab. 3.2. Material Properties for P92. [9]	12
Tab. 4.1. Testing matrix.	19
Tab. 4.2. Testing matrix for CFCG tests.	22
Tab. 4.3. Test matrix of CCG tests.	24
Tab. 4.4. Calculated values for specimen 6, 7, and 8.	30
Tab. 4.5. Locations at which void density analyses were conducted.	37

NOMENCLATURE

a = instantaneous crack length at a given voltage

a_o = initial crack length of specimen for crack length equation

a_i = initial crack length after precrack

a_f = final crack length of specimen

\dot{a} = the crack growth rate

B = specimen thickness of a compact tension specimen

B_N = net thickness of a compact tension specimen

C^* = contour integral creep crack growth

$(C_t)_{avg}$ = contour integral for creep fatigue crack growth

E = modulus of elasticity

K = stress intensity factor

P = applied load for compact tension specimens

$f\left(\frac{a}{W}\right)$ = function of crack length and width

$\sigma_{refPL\sigma}$ = plane stress reference stress

$\sigma_{refPL\epsilon}$ = plane strain reference stress

σ_{ref} = mean of plane stress reference stress and plane strain reference stress

n = Norton Osberg material exponent constant

t_h = hold time

t_T = transition time

U = instantaneous voltage

U_o = initial Voltage of direct current potential drop (DCPD)

U_f = final Voltage of direct current potential drop (DCPD)

ΔV = total load line displacement change

ΔV_c = creep component of the load line displacement change

ΔV_e = elastic component of the load line displacement change

\dot{V} = total load line displacement rate

\dot{V}_c = creep component of the load line displacement rate

\dot{V}_e = elastic portion of the load line displacement rate

ν = Poisson ratio

W = specimen width

λ = non-dimensional crack velocity

1. INTRODUCTION

High chromium heat resistant steels, such as P92, are commonly used for boiler components that are operated around 600°C in ultra-supercritical (USC) thermal power plants. 22% of electricity generation in the US is from coal-based steam power plants [16]. Supercritical (SC) is when water ceases to boil and moves directly from liquid to superheated steam since the main steam pressure is above the thermodynamic critical point of water. Ultra-supercritical (USC) is when the main and reheat steam temperature is much higher than the conventional subcritical steam plants and exceeds 600°C. A coal boiler steam power plant's efficiency is typically 32% to 42%. The results of a USC power plant are more efficient with lower air emissions than a SC power plant, with an efficiency level reaching up to 42%. These high steam temperatures and pressures require a specialized pipe metallurgy to be used in boiler components. [17]

The boiler is an imperative component to a steam power plant. The coal-fired boiler converts water into superheated steam that is delivered to a steam turbine. A waterwall is a wall of welded tube panels that makes up the furnace where fuel with preheated air is burned. Gases produced from combustion flow through the furnace which then evaporates the water within the waterwall tubes into steam. The steam is then superheated in a superheater section which is then delivered via the main steam pipes to the turbine. Low pressure steam exhausted from the high-pressure turbine are reheated in a reheater and provided to the low-pressure turbine through reheat pipes [15]. [10, Fig 1.1] shows an example of a header pipe.

Two commonly researched and used materials in boiler components are P91 and P92 steel. These two materials are commonly used in the high temperature header pipes and steam leads due to their creep properties at elevated temperatures. However, P92 has shown better high temperature creep resistance and creep strength than P91 and is the material of interest in this study since there is not as much research and data collected on it.



Fig. 1.1. Example of a boiler header pipe. [10]

Creep fatigue crack growth (CFCG) and creep crack growth (CCG) of P92 at 650°C are studied. It is important to know how damage and crack growth occurs within the header pipe to evaluate their service life capabilities either after manufacturing or after many years in service. Fracture and damage mechanics methods are implemented to characterize the CFCG and CCG using standard compact tension (CT) specimens. An analysis of whether these samples from a header pipe should be characterized using the stress intensity factor, K , the contour integral, C^* , or $(C_t)_{avg}$ is conducted, as well as an analysis of if this material behaves in a creep ductile or creep brittle manner.

2. LITERATURE REVIEW

2.1 Fracture Mechanics

Fracture mechanics problems are classified into the following three categories: linear-elastic fracture mechanics (LEFM), elastic-plastic fracture mechanics (EPFM), and time-dependent fracture mechanics (TDFM) regimes. These classifications are based on the dominant operating deformation modes in the cracked bodies [1]. The basis of LEFM and the development of the stress intensity factor, K , was founded by Griffith and Irwin almost a century ago. Griffith showed that the square root of crack length and the fracture stress demonstrated an inverse relationship through experiments on brittle materials such as glass. Through these experiments, Griffith was able to develop an equation for crack growth by relating the material properties of glass, the far field stress, and the square root of crack length [1] [2].

Irwin later modified Griffith's equation with a relation of the energy release rate, G , to K to quantify the crack tip driving force. K depends on the mode of crack displacement, loading, crack shape, and component configuration. There are three distinct modes of loading that are shown in [1, Fig. 2.1]. Mode I is the crack opening mode and is loaded perpendicular from the crack plane. Mode II and Mode III are shear loadings with Mode II being sliding in-plane shear and Mode III being tearing out-of-plane shear. A combination of the three modes (I, II, III) is known as mixed loading. This study will focus on pure Mode I loading since it is the most common and most studied [2].

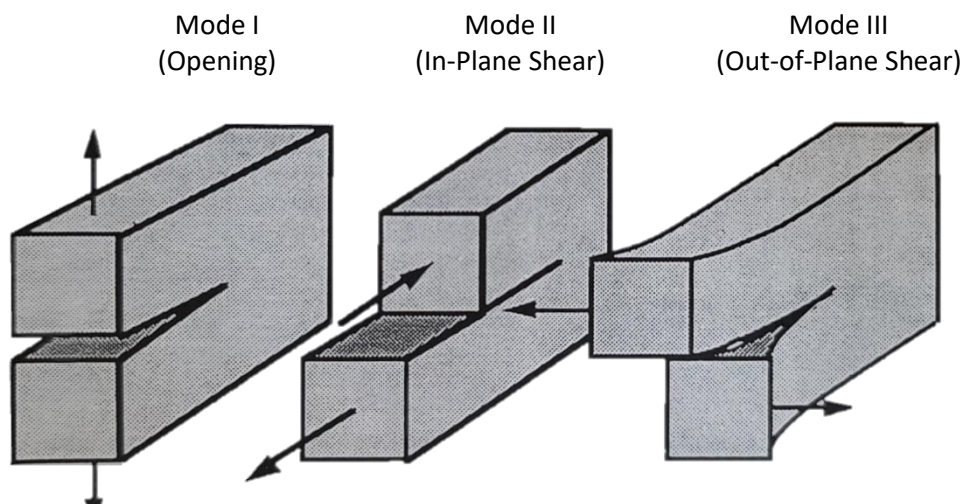


Fig. 2.1. Three modes of loading. [2]

The general K equation developed by Griffith and Irwin for Mode I is:

$$K = \sigma\sqrt{\pi a}f\left(\frac{a}{W}\right) \quad (2.1)$$

[3, eq. (2.2)] is the specific stress intensity equation for a compact tension (CT) specimen used in this study.

$$K = \frac{P}{(BB_N)^{\frac{1}{2}}W^{\frac{1}{2}}}f\left(\frac{a}{W}\right) \quad (2.2)$$

P is the load, B is the specimen thickness, B_N is the net thickness after side groovings if required, W is the specimen width, and $f\left(\frac{a}{W}\right)$ is a function of crack length and width represented by

$$f\left(\frac{a}{W}\right) = \left[\frac{2 + \frac{a}{W}}{\left(1 - \frac{a}{W}\right)^{\frac{3}{2}}} \right] \left(0.866 + 4.64 \left(\frac{a}{W}\right) - 13.32 \left(\frac{a}{W}\right)^2 + 14.72 \left(\frac{a}{W}\right)^3 - 5.6 \left(\frac{a}{W}\right)^4 \right) \quad (2.3)$$

When creep strains become larger, LEFM is unable to predict crack growth. TDFM concepts are used when the stress-strain and load-displacement behaviors are time-dependent due to either time-dependent creep or dynamic loading [1].

2.2 Creep

Creep is non-reversible deformation that is time and temperature dependent. When materials are loaded for long periods of time with a stress lower than their yield strength, creep can occur. Creep typically depends on a material's melting temperature, T_m , and usually starts at approximately 0.3 to 0.5 T_m . When creep occurs, damage in the form of internal cavities conglomerate, typically along the grain boundaries. [4, Fig. 2.2] is a deformation mechanism diagram that summarizes the range of stress and temperature when each type of creep can occur [4].

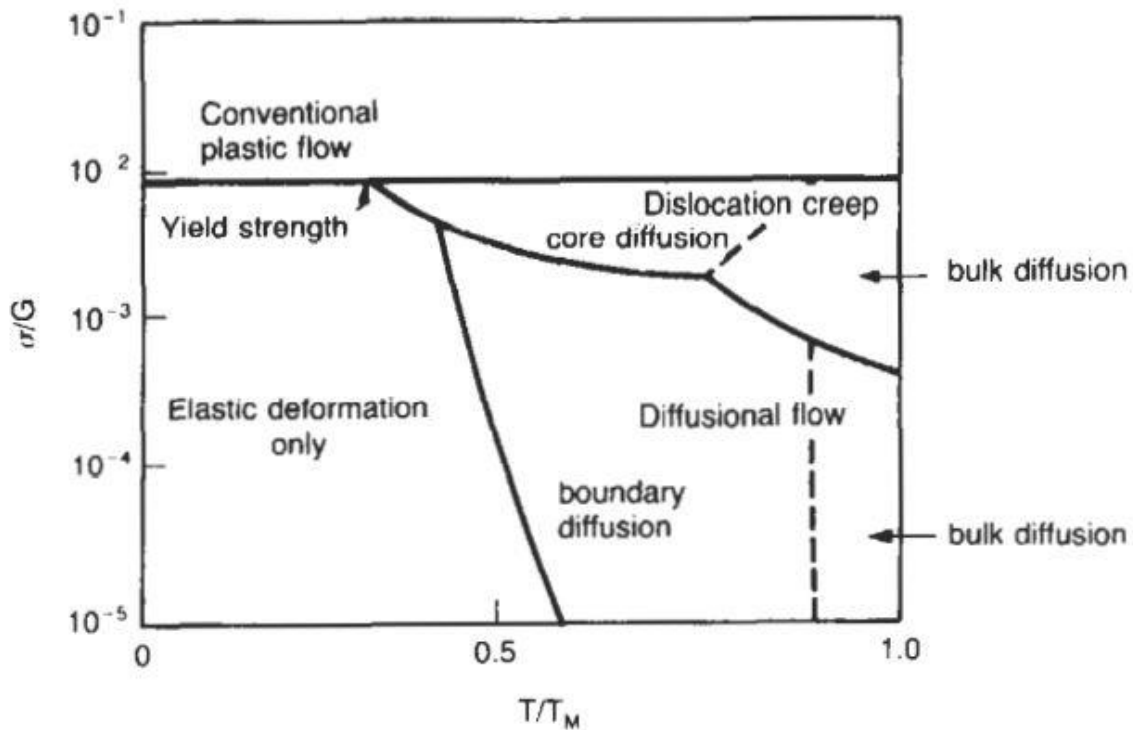


Fig. 2.2. Deformation mechanisms at different stresses and temperatures. [4]

As a material is heated to $0.3T_m$ and loaded, atoms can start to move around or diffuse. There is bulk diffusion that can be split into interstitial and vacancy diffusion, and there are fast diffusion paths that can be split into grain boundary and dislocation core diffusion. Interstitial diffusion is shown in [7, Fig. 2.3(a)] and is when small atoms diffuse from one interstice to another when they have enough energy. Carbon, oxygen, nitrogen, boron and hydrogen diffuse interstitially in most crystals and can diffuse quickly. [7, Fig. 2.3(b)] shows vacancy diffusion which is the second bulk diffusion mechanism. Vacancy diffusion is a mechanism by which most diffusion in crystals takes place and is when a bigger atom that cannot fit into interstices has to wait for a missing atom, known as a vacancy, to appear next to it before diffusing. [7, Fig. 2.3(a) and 2.3(b)] show the two fast diffusion paths: grain boundary diffusion and dislocation core diffusion, respectively. These mechanisms can have a local diffusion rate up to 10^6 times greater than bulk diffusion. Creep mechanisms can be split into two categories, dislocation creep and diffusion creep. At higher stresses, dislocation creep is the dominating mechanism and, as the stress is reduced, creep does not stop but rather switches mechanisms to diffusion creep [4].

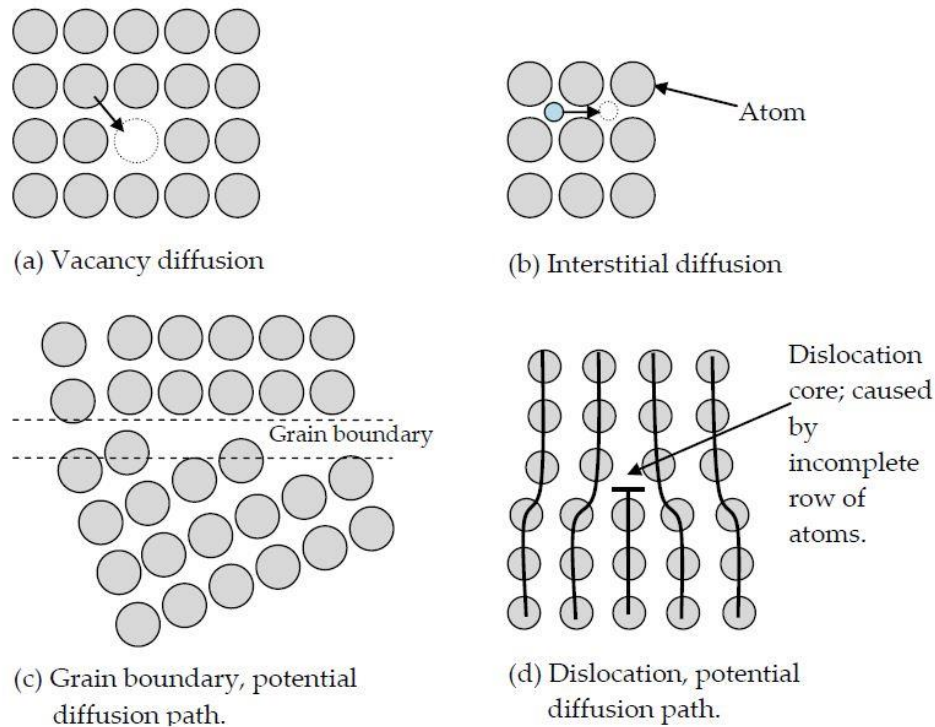


Fig. 2.3. Creep mechanisms. [7]

Creep deformation is typically divided into three time periods or stages which are small-scale creep (SSC), transition creep (TC), and extensive creep (EC). [1, Fig. 2.4] shows each of these stages under a constant applied force. In the small-scale creep region, see [1, Fig. 2.4(a)], there is only a small section of uncracked ligament near the crack tip that sees creep deformation [1] [13]. Under small-scale creep conditions, the contour integral C_t can be used to calculate crack growth. The equation for C_t is given in ASTM E1457 [3] as:

$$C_t = \frac{P\dot{V}_c}{\sqrt{BB_N}W} \frac{F'}{F} \quad (2.4)$$

where

$$\frac{F'}{F} = \left[\frac{1}{2 + \frac{a}{W}} + \frac{1}{2 \left(1 - \frac{a}{W}\right)} \right] + \frac{f'}{f} \quad (2.5)$$

f is defined in [3, eq. (2.3)] and f' is defined as:

$$f' = 4.64 - 26.64 \left(\frac{a}{W}\right) + 44.16 \left(\frac{a}{W}\right)^2 - 22.4 \left(\frac{a}{W}\right)^3 \quad (2.6)$$

\dot{V}_c is the creep load line displacement rate which is calculated by:

$$\dot{V}_c = \dot{V} - \dot{V}_e \quad (2.7)$$

where \dot{V} is the total load line displacement rate and \dot{V}_e is the elastic portion of the load line displacement rate which is defined as:

$$\dot{V}_e = \frac{2B\dot{a}K^2(1-\nu^2)}{PE} \quad (2.8)$$

for plane strain. Where \dot{a} is the crack growth rate, ν is Poisson's ratio and E is the elastic modulus of the material. If the specimen has side grooves, then the net thickness, B_N , is used in replacement of B [5].

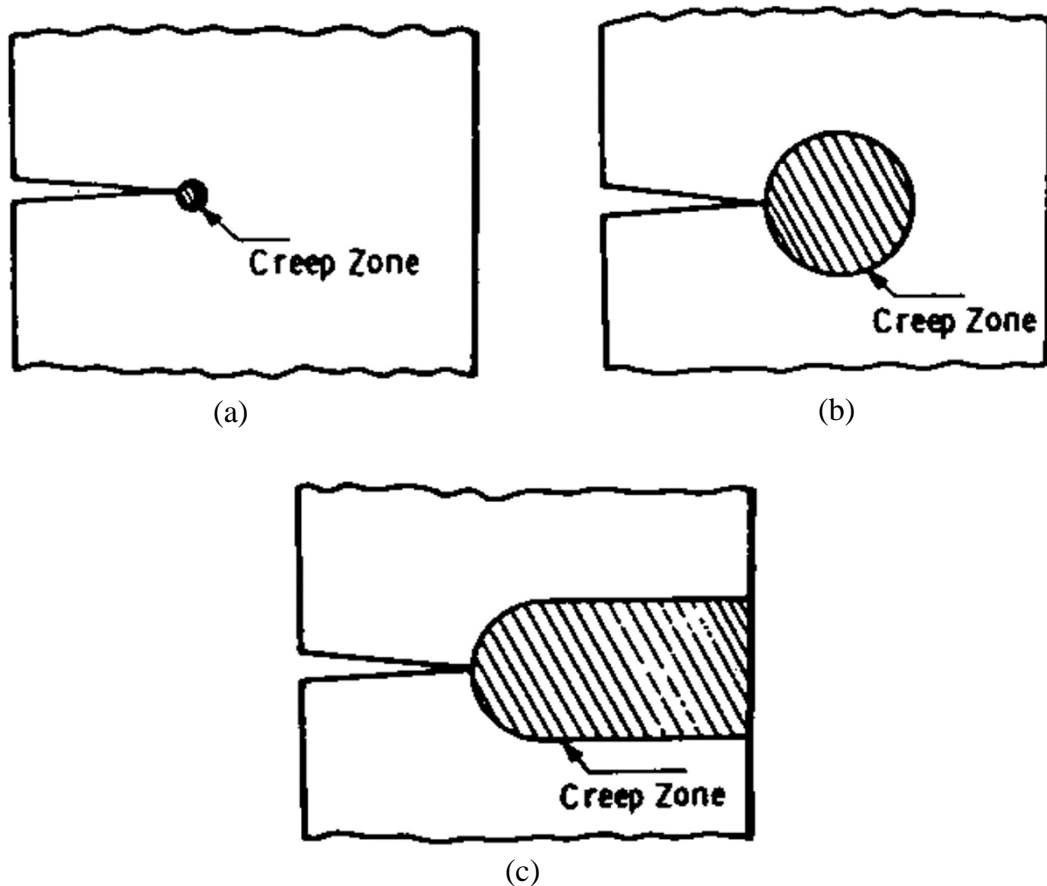


Fig. 2.4. Schematic representation of the levels of creep deformation under which creep crack growth can occur. Small Scale Creep (a), Transition Creep (b), Extensive Creep (c). Adapted from [1]

The transition creep deformation region is shown in [1, Fig. 2.4(b)] and dominates the elastic and plastic zones. However, this region does not dominate the whole uncracked ligament of the component. C_t is typically a higher value than the contour integral C^* and as

time elapses it becomes equal in value once it reaches steady-state creep [8] [13]. The time that C_t becomes equal to C^* is defined as the transition time. ASTM E-1457 [3] gives the equation for transition time as follows:

$$t_T = \frac{K^2(1 - \nu^2)}{E(n + 1)C^*(t_T)} \quad (2.9)$$

where, n is the Norton Osberg material exponent constant, t is the time, and C^* is the contour integral for steady-state creep given by [3, eq. (2.10)].

ASTM E1457 [3] states that only data for which the time exceeds transition time, t_T , are valid by this test method. t_T is estimated by the equation above. The calculation of t_T depends on the value of $C^*(t_T)$. Thus, the following procedure must be used for its estimation. For time, t , corresponding to each data point, calculate t'_T using the above equation but substituting $C^*(t)$ for $C^*(t_T)$. t_T is then the largest value of t'_T in the entire data set.

Extensive creep or steady-state creep occurs when the creep deformation region dominates the entire uncracked ligament of the component as seen in [1, Fig. 2.4(c)]. The contour integral C^* , for compact CT specimens, defined by [3, eq. (2.10)] is used to calculate crack tip parameter values that will be correlated to creep crack growth rates. \dot{V}_c is a function of time which means C^* is a function of time and can be denoted as $C^*(t)$ [3] [8] [13].

$$C^*(t) = \frac{P\dot{V}_c}{B_N(W - a)} \frac{n}{n + 1} \left(2 + 0.522 \frac{W - a}{W} \right) \quad (2.10)$$

2.3 Creep Crack Growth Parameters

The three parameters that are used to correlate the creep crack growth rates in cracked bodies are the stress intensity factor (K), the contour integral (C_t), and the steady state contour integral (C^*). C^* and C_t are used for creep ductile materials, C_t for small-scale creep, and C^* for extensive creep. K is used for creep brittle materials [7]. For creep brittle materials, crack growth propagates with low ductility where creep strains are less than or comparable to the elastic strains near the crack tip. For creep ductile materials, crack growth is characterized by time-dependent creep strains that dominate the elastic strains near the crack tip [14].

By relating crack growth versus time to the creep displacement versus time, different characteristics can be observed between creep-ductile materials and creep-brittle materials. Yokobori showed this distinction by comparing Cr-Mo-V steel, a high temperature creep ductile material, with IN100 alloy, a high temperature creep brittle material. He noticed that the correlation between creep crack growth rates, da/dt , and the contour integral, C^* , varied between these two materials. The Cr-Mo-V steel had a non-unique correlation in the lower creep crack growth region which typically occupies 30-40% of the total creep fracture life. The IN100 alloy showed a tendency for the crack growth rate, da/dt , and contour integral, C^* , to decrease initially. This region near the lowest da/dt values is where the data was concentrated and occupies 80-90% of the total creep fracture life [8].

These characteristic differences between creep-brittle and creep-ductile materials are due to differences in creep crack growth (CCG) and load line displacement (LLD) behaviors. Yokobori [8] plotted creep crack growth curves based on CT specimens for Cr-Mo-V steel and IN100 alloy against non-dimensional time (t/t_f) where t_f is the creep fracture life for each specimen as shown in [8, Fig. 2.5]. He showed that for Cr-Mo-V steel, acceleration in the creep crack growth rate occupies approximately 60% of the total creep fracture life and begins at an early stage of the creep fracture life. The IN100 alloy's curve showed a linear relationship between non-dimensional time and creep crack growth that occupies most of the creep fracture life, about 80%, and the accelerating portion only occupies 10% of the total life. This region is the steady-state region where creep crack growth rate attains a constant value and is determined by the initial stress intensity factor, K [8].

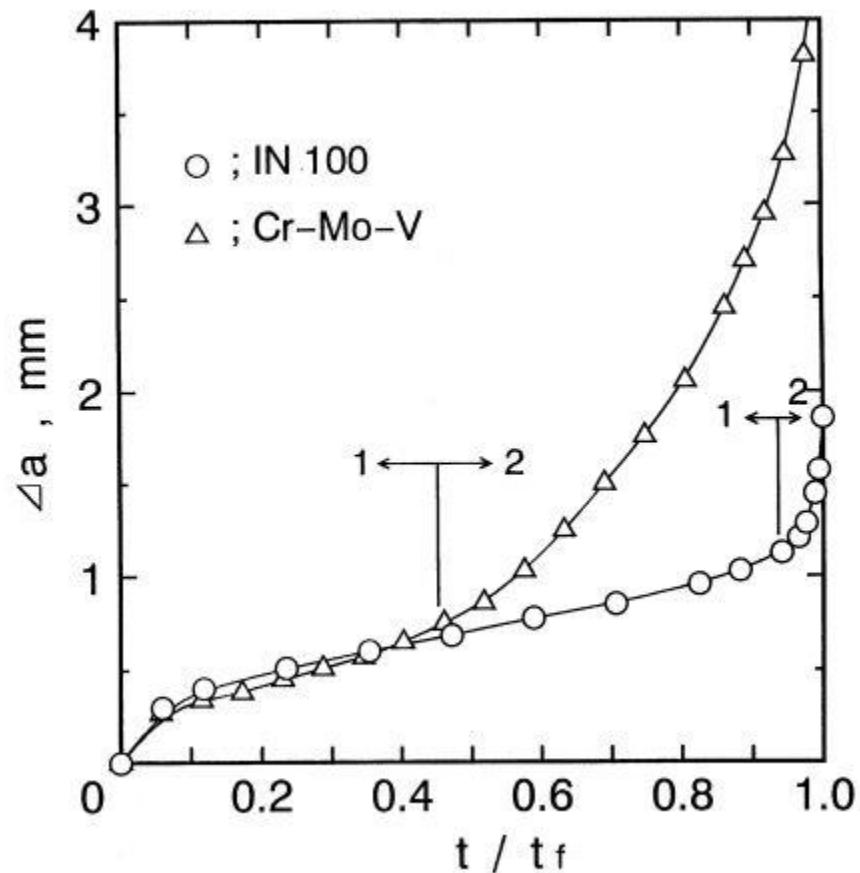


Fig. 2.5. Comparison of crack length Δa vs t/t_f between Cr-Mo-V steel and IN 100. 1 and 2 correspond to uniform velocity portion and accelerating portion, respectively; t_f = creep fracture life. [8]

Tabuchi *et al.* [9] conducted creep crack growth (CCG) experiments on P92 steel comparing weld materials to the base metal at 600°C, 625°C, and 650°C as part of a Japanese round robin study. When comparing the welded material to the base metal, Tabuchi *et al.* [9] found that under the same testing conditions the deformation is initially roughly the same for the two. However, the acceleration of crack growth occurred at a lower deformation and had a shorter life for the welded material compared to the base material. [9, Fig. 2.6] shows the two load line displacement curves for the welded and base material. Tabuchi *et al.* [9] also noticed that the welded material showed more creep brittle failure compared to the base material that was observed to be more ductile. Therefore, in studies developed to explore the creep and creep fatigue crack growth behavior, it is important to understand the mechanisms that drive the material to behave in a creep ductile or creep brittle manner. The details of the materials used

by Tabuchi *et al.* are discussed further in Section 4.4 and the specific specimen geometry and material composition that is analyzed in this study will be discussed in the following chapter.

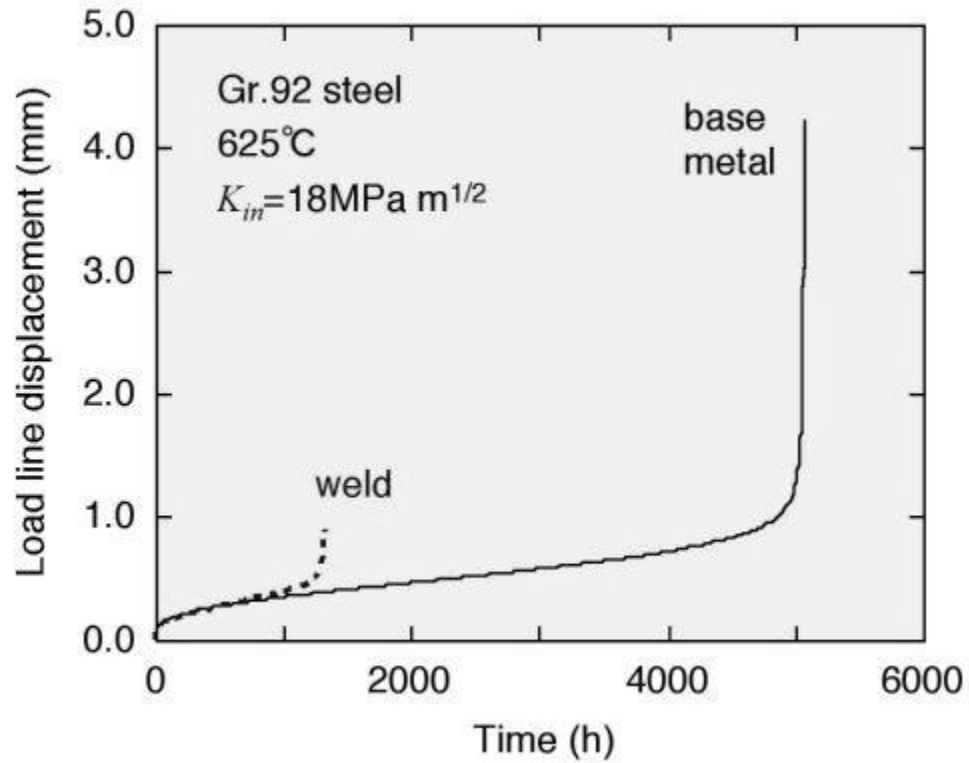


Fig. 2.6. Comparison of load-line displacement of the weldment and base metal. [9]

3. EXPERIMENTAL DETAILS

3.1 Material and Specimen Geometry

The material evaluated in this research is ASME steel grade P92 in the tempered martensitic condition and was provided by Electrical Power Research Institute (EPRI). This high chromium steel has added Tungsten (W) and reduced Molybdenum (Mo) compared to ASME steel grade P91, which helps increase high temperature creep and oxidation resistance. The approximate material composition and material properties at 650°C are listed in [10, Tab. 3.1], [9, Tab. 3.2], respectively. This material composition is also analyzed later in Chapter 4 using the scanning electron microscope mentioned in Section 3.2. The as-received blanks were machined in the same orientation and position from header pipe material.

A standard compact tension (CT) specimen was used for all tests with dimensions: $W = 50.7$ mm, $B = 12.7$ mm, $a_n = 10$ mm. All other dimensions are defined in Fig. 3.1. These CT specimens were machined using electrical discharge machining (EDM) in order to cut the specimen geometry in an accurate and repeatable manner. The specimen notch shown in Fig. 3.1, denoted as a_n , is oriented in the length direction of the P92 header pipe so that the loading direction of the specimen is in the circumferential direction.

Tab. 3.1. Material composition from EPRI. [10]

P92	Al	As	B	Bi	C	Ca	Co	Cr	Cu	La	Mn	Mo	N
Min%	0.000	0.0000	0.0000	0.000	0.000	0.0000	0.000	0.00	0.000	0.000	0.00	0.00	0.0000
Max%	<0.002	0.0073	0.0033	<0.00001	0.105	0.0011	0.141	8.91	0.141	<0.002	0.45	0.38	0.0475
Nb	Ni	O	P	Pb	S	Sb	Si	Sn	Ta	Ti	V	W	Zr
0.000	0.00	0.0000	0.000	0.00000	0.0000	0.0000	0.000	0.000	0.000	0.000	0.000	0.0	0.000
0.058	0.37	0.0043	0.013	0.00009	0.0051	0.0015	0.269	0.01	<0.002	<0.002	0.158	1.7	<0.002

Tab. 3.2. Material Properties for P92. [9]

Material	E (Gpa)	σ_{ys} (Mpa)	A (Mpa ⁻ⁿ h ⁻¹)	n
P92	85	126	3.77E-19	6.71

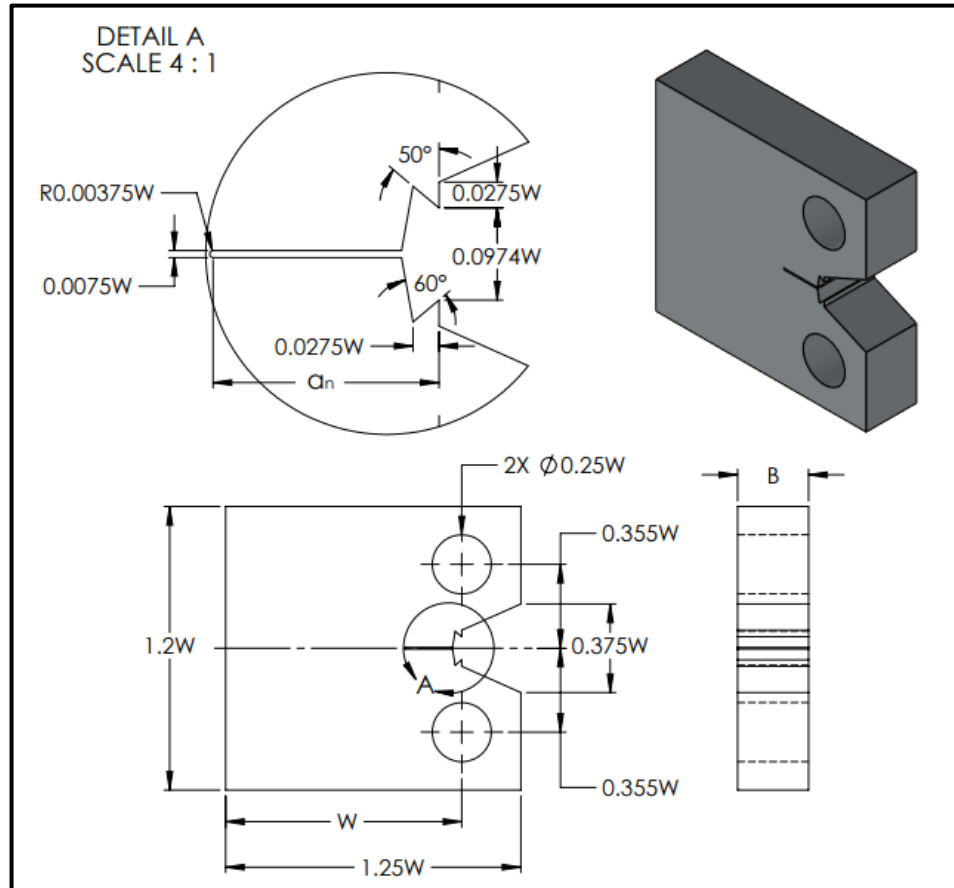


Fig. 3.1. Specimen geometry.

3.2 Experimental Testing Equipment

All experiments were conducted on one of the following: MTS 312.11 44 kN (10 kip) servo-hydraulic load frame, MTS 312.12 97 kN (22 kip) servo-hydraulic load frame, or a deadweight creep frame. The three frames are shown in Fig. 3.2. The MTS servo-hydraulic load frames were controlled using an MTS 458.20 MicroConsole with an MTS 458.91 MicroProfiler. A program within the MicroProfiler was created to control the desired CFCG experiments' waveform. The deadweight creep frame was fabricated in our research lab starting with a commercially purchased 20-ton shop press frame that was modified. The top crossbar member was machined so that the load train extended vertically from the top member to the bottom member. The bottom crossbar member has a machined plate attached to the bottom for the load train to be tightened accordingly. All major load train components were machined in the University of Idaho ME Machine Shop. These include top and bottom IN 718 threaded rods, grips, and pins. Multiple components were added to this to complete the

deadweight creep frame including: a 30:1 inch lever arm to apply the proper load, an Optima 44 kN (10 kip) load cell with a digital read out for constant load monitoring, an extensometer which is described later in this section, and two dial indicators positioned along the upper portion of the load train to confirm load line displacement readings from the extensometer.



Fig. 3.2. Load frames from left to right: MTS 312.11 44 kN (10 kip), MTS 312.12 97 kN (22 kip), deadweight creep frame.

Each test was conducted at 650°C as requested by Electrical Power Research Institute (EPRI). To maintain this constant temperature throughout each test, an Applied Test Systems (ATS) split case furnace was attached to the creep or MTS frames with the specimen placed in the center of the furnace. According to ASTM standard E-21, the temperature variation of the specimen must not exceed $\pm 3^{\circ}\text{C}$ [18]. Depending on the test frames, either an ATS temperature control system or a Watlow series 981 temperature controller was used as the temperature controller. A thermocouple was spot welded on the back side of the specimen above the crack plane as shown in Fig. 3.3 with a k-type thermocouple wire. To confirm the temperature the controller displayed, an external thermocouple was used to measure the specimen's temperature at various points on the specimen.

Throughout the experiments, crack length was measured in two different ways. The first used the direct current potential drop method (DCPD). This method uses a Keithley

2280S-32-4 Precision Measurement DC Supply to supply a voltage through the CT specimen while a Keithley 2182A Nanovoltmeter reads the voltage drop across the crack as it propagates. The DC power supply is wired to the specimen using two different wires. The first is the positive wire which is spot welded to the top of the notch side face as shown in Fig. 3.3, denoted as A+. The second wire is the ground wire and is spot welded to the bottom of the notch side face as shown in Fig. 3.3, denoted as A-. The DC power supply is set to have a maximum current output of 2 amps. The nanovoltmeter is connected to two wires that are spot welded to the specimen: the positive wire on the front side above the notch, denoted as B+, and the negative wire on the back side below the notch, denoted as B-. As the crack propagates, there is less material for the current to flow through, which increases the resistance to electrical flow. As a result, the differential voltage between B+ and B- increases. This DCPD method of analyzing the voltage change as the crack grows can be directly correlated to how the crack length is calculated at any point throughout the experiment using [6, eq. 3.1].

$$a = \left[(a_f - a_o) \frac{(U - U_o)}{(U_f - U_o)} \right] + a_o \quad (3.1)$$

Where a is the instantaneous crack length at a given voltage, a_o is the initial crack length of the specimen, a_f is the final crack length of the specimen, U is the instantaneous potential drop between B+ and B-, U_o is the initial voltage of the DCPD, and U_f is the final voltage of the DCPD.

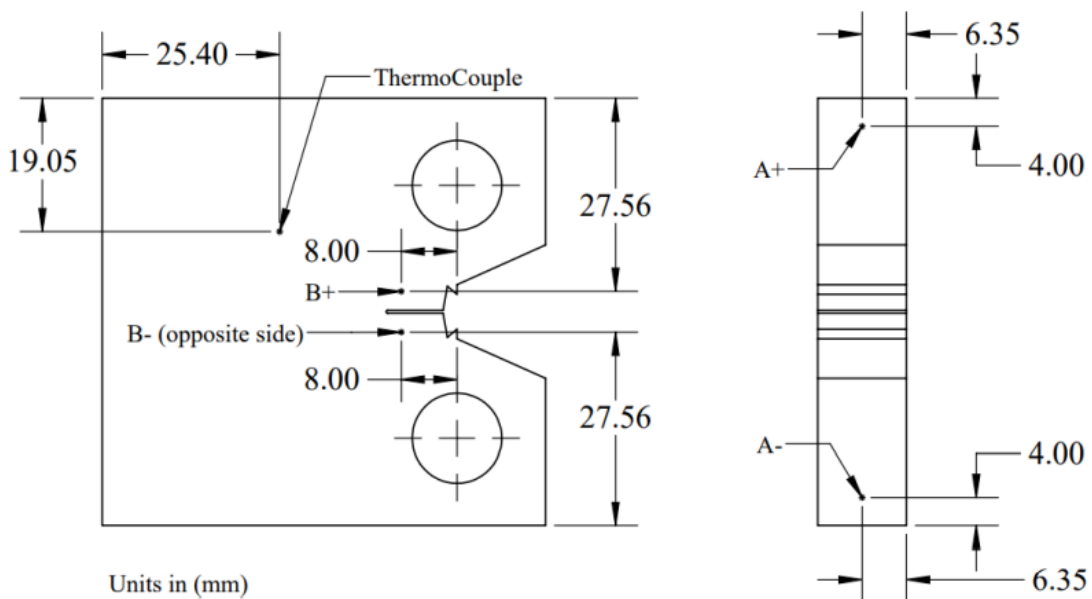


Fig. 3.3. DCPD spot welding locations.

The second method used to measure crack growth during a test was through visual tracking using a camera lens positioned on an x-y translator with a resolution of 0.01 mm. This method only measures surface crack length while the DCPD method averages the crack length through the thickness of the specimen.

To calculate \dot{V}_c and C^* as presented in Chapter 2, LLD was recorded using an MTS 632.11 B-20 axial high temperature extensometer. The extensometer was equipped with two ceramic rounded stepped end rods to reach the knife edges of the specimen through the side of the split case furnace. The placement of the extensometer on the knife edges is shown in Fig. 3.4.

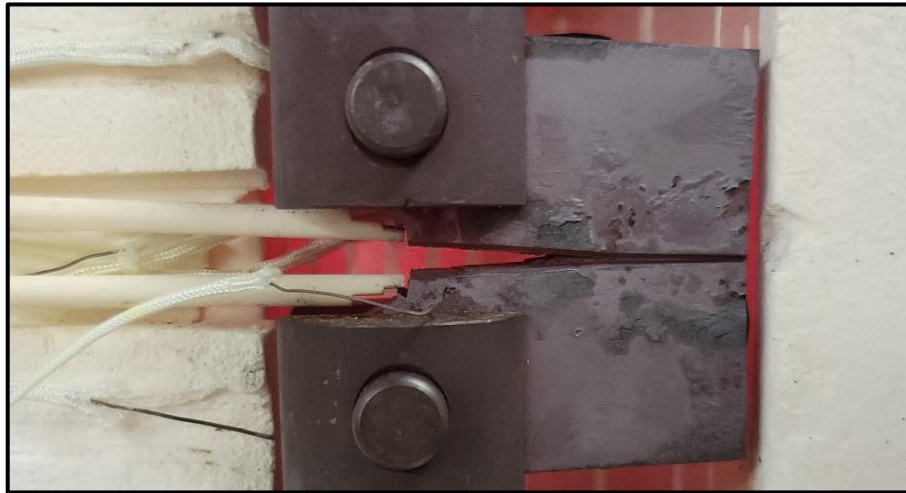


Fig. 3.4. Extensometer knife edge placement.

Once a test was finished, fractography on the fracture surface and below the crack front was performed. A Zeiss Supra 35 VP scanning electron microscope (SEM) was used for secondary electron imaging. A secondary attachment on the SEM allowed for energy dispersive X-ray spectroscopy (EDS) and backscattered electron imaging (BSE) to be used in post processing. This is further discussed in Chapter 4.

3.3 Testing Procedures

Before the specimens were tested, they were polished to 1 μm grit to help track the precrack length visually while load shedding to the desired starting stress intensity factor, ΔK for CFCG and K_{max} for CCG tests. Load shedding procedure for each specimen was performed in accordance with ASTM E-647 [12] at a rate of 15 Hz. A starting notch length of $a_i = 10$ mm and ending precrack length of 18 mm was desired with a starting K_{max} around $31 \text{ MPa}\sqrt{(\text{m})}$

and an end K_{max} range of 15 to 24 $\text{MPa}\sqrt{\text{m}}$ using a 15 Hz sinusoidal waveform. The various ending range of K_{max} was dependent on the type of test being performed.

Two different types of experiments were the focus of this research. These include creep fatigue crack growth (CFCG) with a 60 s hold time and creep crack growth (CCG). CF CG tests were conducted with a trapezoidal waveform with an unloading and loading time of 0.25 s and a hold time of 59.5 s. CCG tests were held at a constant load for the duration of the test. Fig. 3.5 shows the 15 Hz, 60 s hold and creep test waveforms.

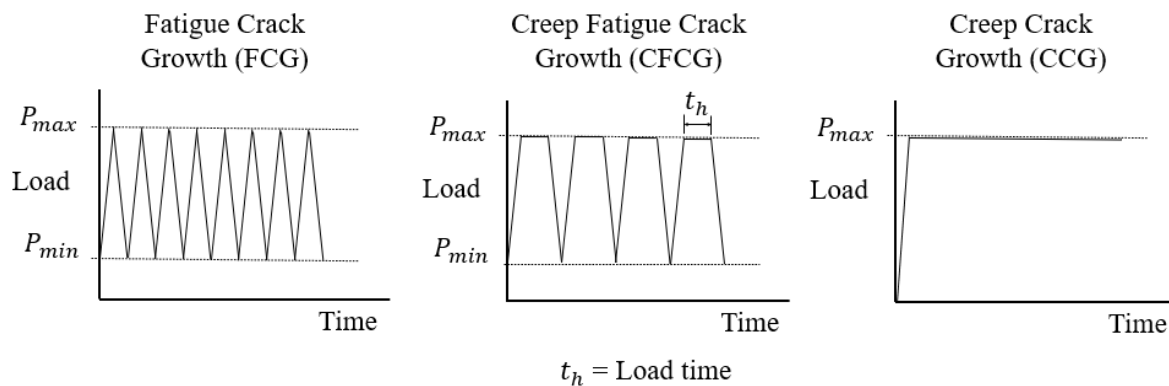


Fig. 3.5. Test waveforms.

When the specimens achieved rapid crack growth leading to imminent failure, the test was stopped. Then the specimens were cooled down to room temperature and fatigued at 15 Hz until fracture. Cooling the specimen to room temperature allowed the final crack length for the test to be found by adding a heat tint to the fracture surface. The two halves were then removed from the load frame and the fracture surfaces were examined under an optical microscope to determine the initial and final crack lengths. Initial and final crack lengths were found by averaging 5 evenly spaced points that measure the length of the precrack or final crack length along the crack front. All plots of data that are shown use these calculated crack lengths and the DCPD data using a 7-point secant method as suggested in ASTM E-647 [12].

For this study, a total of 9 experiments were performed. The first was a baseline 15 Hz FCG test with an initial crack length of $a_i = 18$ mm and an initial stress intensity of $\Delta K = 18$ $\text{MPa}\sqrt{\text{m}}$, a stress ratio (R) of 0.1 and temperature of 650°C. Once the baseline test was completed and analyzed, three additional CF CG tests with a 60 s hold time and five CCG tests

were conducted. Three of the CCG tests (specimen 6, 7, and 8) were sent to EPRI for sectioning using EDM. These samples were mounted in a conductive epoxy and polished. These polished samples allowed for analysis below the fracture surface using the SEM. P92 is known to oxidize, thus looking at the fracture surface directly with the SEM is not as desirable as looking below the fracture surface, i.e. the machined and polished sample. This will be discussed and shown in more detail in Chapter 4.

4. RESULTS AND DISCUSSION

4.1 Testing Matrix

Tab. 4.1 shows details of the 9 experiments performed and a summary of their results. After performing both CFCG and a CCG tests with no side grooves, as recommended by EPRI, the fracture surfaces showed crack tunneling. This will be discussed in more detail in a later section. However, due to the tunneling observed, a series of side groove tests were performed to identify the best side groove percentage for a uniform crack front growth. The fracture surfaces for all the tests conducted are shown in Fig. 4.1 with crack growth going from the bottom of the image to the top of the image. The transition of final fracture to cyclic loading region can be seen in Fig. 4.1. The fracture surface transitions from dark gray to light gray, which correlates respectively to the test fracture surface and the post-test cyclic loading.

Tab. 4.1. Testing Matrix.

Specimen ID	Hold time (s)	Max load (kN)	ΔK_i (MPa \sqrt{m})	ΔK_f (MPa \sqrt{m})	$K_{max,i}$ (MPa \sqrt{m})	$K_{max,f}$ (MPa \sqrt{m})	a_i (mm)	a_f (mm)	Cycles (N_f)	Time (hr)	Side Groove
1	15 Hz	8.89	18.52	47	20.58	52.24	18.40	32.90	42709	0.75	N/A
2	60	9.81	21.29	38.55	23.65	42.83	19.28	29.26	9980	167	N/A
3	∞	10.79	N/A	N/A	24.40	44.53	19.20	28.42	N/A	373	N/A
4	60	8.78	20.02	45.61	22.25	50.68	18.08	31.44	12157	204	20% Total
5	∞	9.48	N/A	N/A	23.15	53.84	17.24	31.20	N/A	480	20% Total
6	∞	8.38	N/A	N/A	21.75	39.47	19.64	29.54	N/A	458	10% Total
7	∞	7.53	N/A	N/A	18.5	35.41	18.54	29.5	N/A	324	10% Total
8	∞	6.70	N/A	N/A	15.57	21.88	17.46	23.88	N/A	1734	10% Total
9	60	9.31	20.62	41.15	22.91	45.73	18.6	30.1	11230	189	10% Total



Fig. 4.1. Fracture surfaces of all nine specimens.

4.2 DCPD vs Crack Length

While doing the procedure described in Section 3.3 to find the initial and final crack lengths, crack front propagation was analyzed. Fig. 4.2 shows three specimens with different side groove percentages, as labeled, with the crack growing from left to right. A side groove is a reduction in the thickness of a specimen along the notch to help the crack propagation occur equally along the crack front. As shown on the top specimen, the no-side-groove specimen's crack front grew quicker in the middle section of the specimen and slower towards the edge of the thickness. This is known as crack tunneling which is not desired. To mitigate this, a 20% total side groove was added after precracking as recommended in ASTM E 647 [12]. Fig. 4.2 shows the no side groove specimen's crack front on the top and the 20% side groove specimen's crack front in the middle. When the 20% total side groove was added, the opposite effect happened. The middle section of the specimen's crack front grew slower while towards the edge of the specimen it grew quicker. Next, a specimen with a 10% total side groove was tested in an attempt at making the crack front propagate evenly throughout the thickness of the specimen. This resulted in a more uniform crack front growth as shown in Fig. 4.2. Since this percentage of side groove proved to be the best amount for a more uniform crack front, the rest of the experiments were side grooved to a total of 10%.

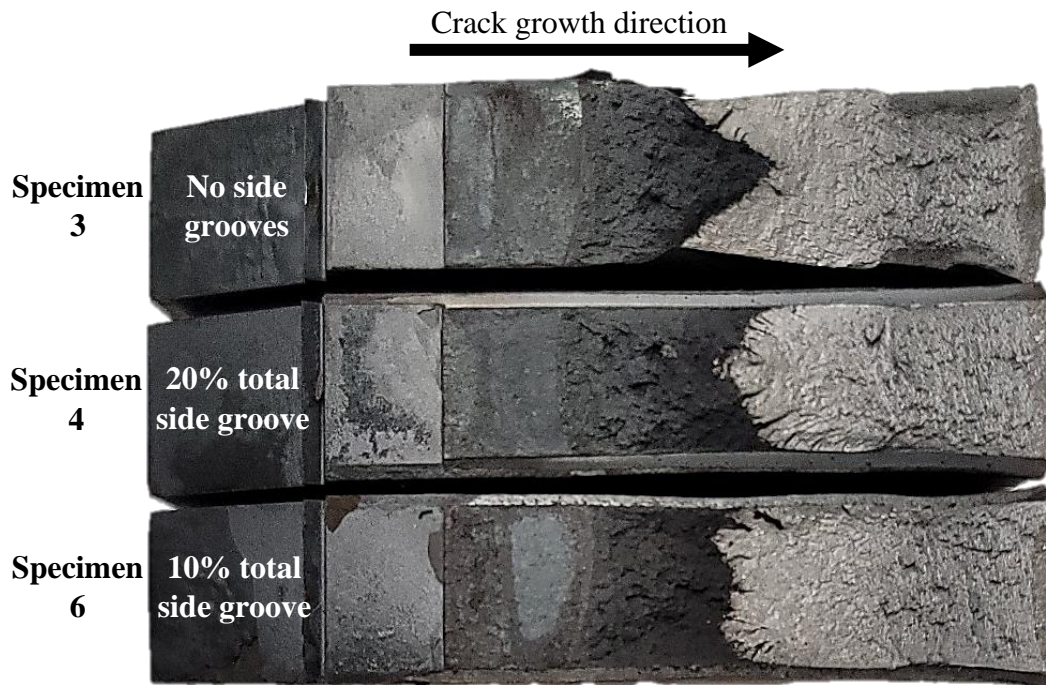


Fig. 4.2. Crack front for three different side groove percentages.

As discussed in Section 3.2, one method of crack length measurement uses the DCPD method. If a normalized DCPD vs. crack length graph, as shown in Fig. 4.3, of an experiment is created, then a semi-accurate estimate of how far a current experiment's crack has grown can be made. The graphs varied from one percentage of side groove to another. These results are shown in Fig. 4.3 with no side groove having the least steep slope and 20% total side groove having the steepest slope. During the experiments, a given crack length can be found using this graph and the line that corresponds to the amount of side groove used. For an experiment, the initial DCPD value can be subtracted from the actual DCPD value which then can be correlated to the DCPD value in the graph to find the current crack length.

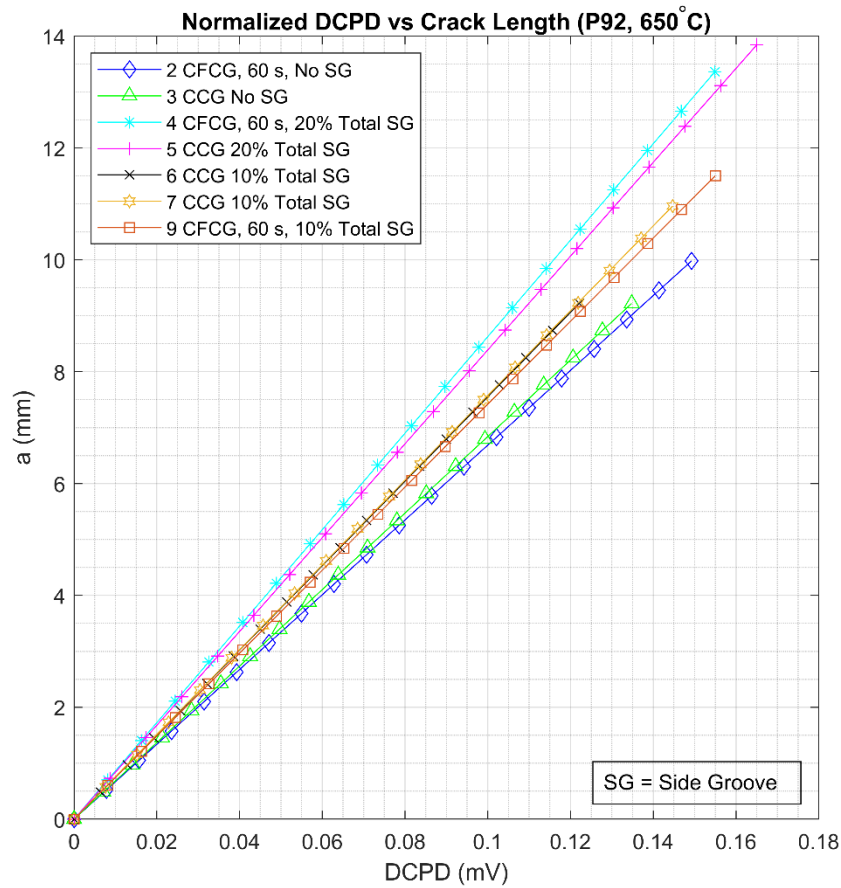


Fig. 4.3. Normalized DCPD vs crack length plot.

4.3 P92 CFCG

Three CFCG tests were conducted at three different side groove percentages and about the same initial ΔK values, as shown in Tab. 4.2, with an R of 0.1 and a hold time (t_h) of 60 s. As discussed in Section 4.2, the different side groove percentages were due to finding the desired side groove percentage needed to make a uniform crack front. However, even though three different side groove percentages were used, once the data was reduced and plotted onto a graph of crack growth rate per cycle, da/dN , as a function of ΔK , each data set collapses onto the same scatter band as shown in Fig. 4.4(a). This shows that the different percentages of side grooves create a different crack front profile yet results in a similar overall crack growth rate as a function of stress intensity.

Tab. 4.2. Testing matrix for CFCG tests.

Specimen ID	Hold time (s)	Max load (kN)	ΔK_i (MPa \sqrt{m})	ΔK_f (MPa \sqrt{m})	$K_{max,i}$ (MPa \sqrt{m})	$K_{max,f}$ (MPa \sqrt{m})	a_i (mm)	a_f (mm)	Cycles (N_f)	Time (hr)	Side Groove
2	60	9.81	21.29	38.55	23.65	42.83	19.28	29.26	9980	167	N/A
4	60	8.78	20.02	45.61	22.25	50.68	18.08	31.44	12157	204	20% Total
9	60	9.31	20.62	41.15	22.91	45.73	18.6	30.1	11230	189	10% Total

Additional comparison can be made with crack growth rate per time, da/dt , as a function of stress intensity, K_{max} , shown in Fig 4.4(b). da/dt can be found from da/dN as shown in [6, eq. (4.1)],

$$\left(\frac{da}{dt}\right)_{avg} = \frac{1}{t_h} \left(\frac{da}{dN}\right) \quad (4.1)$$

where da/dt is the time rate of crack growth and t_h is the hold time. This comparison is important because CCG tests do not have cycles, so, to compare the CFCG to CCG tests, the data needs to be compared as a function of time. Comparing Fig. 4.4(a) and 4.4(b), the 10% side groove test varies a little bit more than the other two towards the end of the test.

Load line displacement (LLD) data were collected for the CFCG experiments using an extensometer as discussed in Section 3.2. These data were collected to calculate the creep load line displacement, ΔV_c , and the creep load line displacement rate, \dot{V}_c , so that C^* can be calculated and compared to the C^* values for the CCG tests. However, due to noise and inaccurate readings within the LLD data, it was not possible to calculate \dot{V}_c . Therefore, the

contour integral, $(C_t)_{avg}$, and the creep load line displacement, ΔV_c , were calculated as shown in [6, eq. (4.2) and (4.3)], respectively.

$$(C_t)_{avg} = \frac{\Delta P(\Delta V_c)}{\sqrt{BB_N W t_h}} \left(\frac{f'}{f} \right) \quad (4.2)$$

$$\Delta V_c = \frac{2B_N t_h (1 - \nu^2) \Delta K^2 \left(\frac{da}{dt} \right)_{avg}}{EP_{max}} \quad (4.3)$$

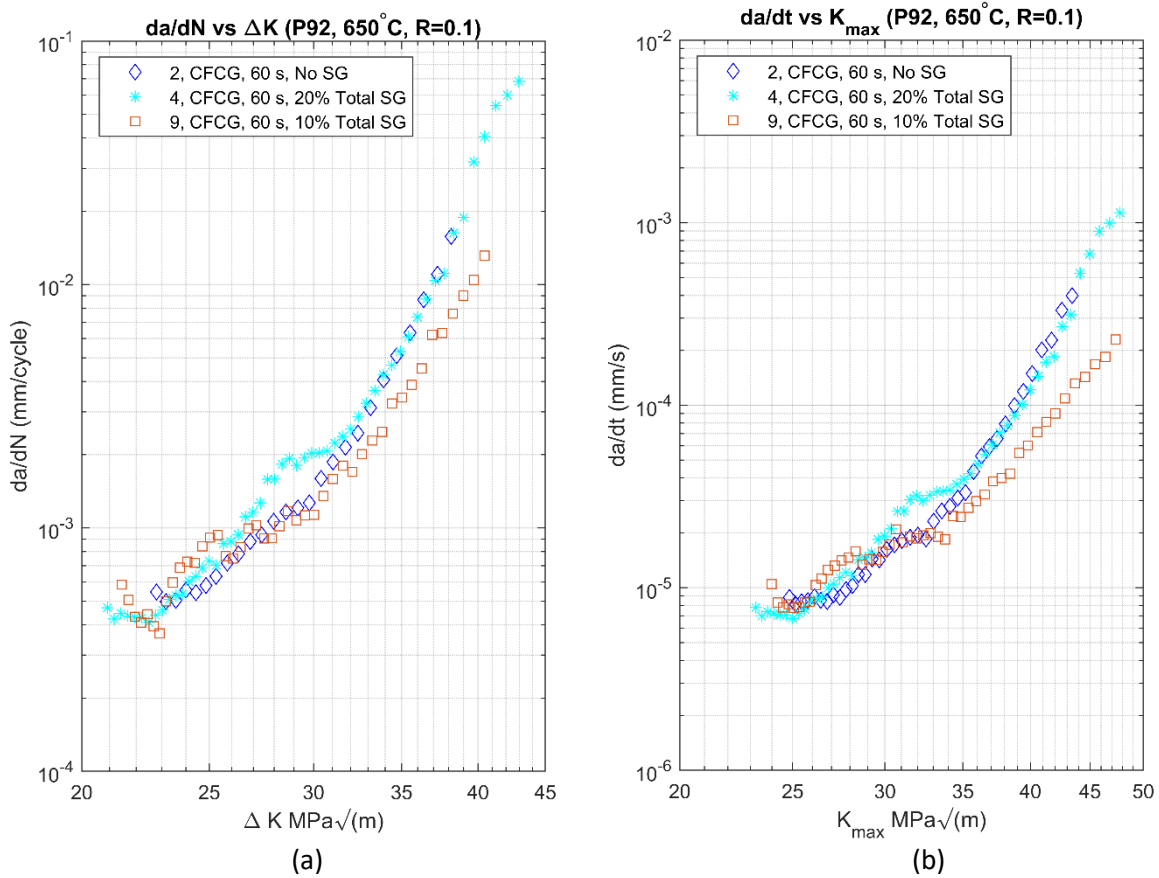


Fig. 4.4. CFCG plots from left (a) da/dN vs Delta K and the right (b) da/dt vs Kmax.

When the three CFCG tests are plotted on a $(C_t)_{avg}$ versus da/dt graph as shown in Fig. 4.5, all three data sets line up. Comparing the two crack growth rate per time plots in Fig. 4.4(b) and 4.5, it can be seen that the contour integral, $(C_t)_{avg}$, correlates the crack growth in all three tests better than the stress intensity factor, K_{max} , as shown in Fig. 4.4(b).

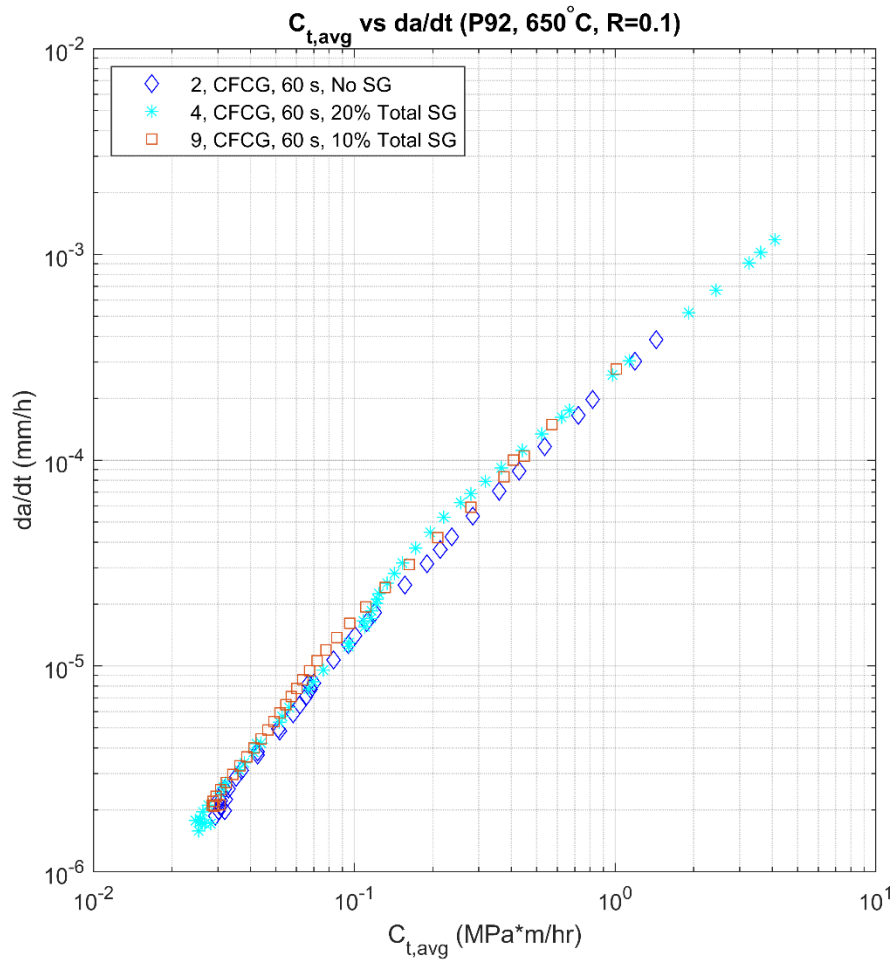


Fig. 4.5. Crack growth rate, da/dt , versus contour integral, $(C_t)_{avg}$.

4.4 P92 CCG

A total of five CCG tests were performed as shown in Tab. 4.3. One goal of this research study was to achieve a 1000-hr plus test since there is very little data available for long term testing at 650°C for parent material P92. To achieve this goal, as the tests progressed from specimen 3 to specimen 8, the initial K_{max} value was lowered to obtain a longer life CCG

Tab. 4.3. Test matrix of CCG tests.

Specimen ID	Max load (kN)	$K_{max,i}$ (MPa√m)	$K_{max,f}$ (MPa√m)	a_i (mm)	a_f (mm)	Time (hr)	Side Groove
3	10.79	24.40	44.53	19.20	28.42	373	N/A
5	9.48	23.15	53.84	17.24	31.20	480	20% Total
6	8.38	21.75	39.47	19.64	29.54	458	10% Total
7	7.53	18.5	35.41	18.54	29.5	324	10% Total
8	6.70	15.57	21.88	17.46	23.88	1734	10% Total

test. Specimen 8 accomplished this goal with an initial K_{max} of about $15.5 \text{ MPa}\sqrt{\text{m}}$ resulting in a test length of 1734 hrs. This test actually ended prematurely due to a power outage.

Fig. 4.6(a) shows a graph of da/dt versus K_{max} for all the CCG tests with the exception of specimen 5. Specimen 5's data collection had issues due to power outages resulting in inconclusive data reduction. Fig. 4.6(b) is a graph of just the 10% total side grooved CCG specimens. One thing to note is that even though specimen 7 started at a lower K_{max} value than specimen 6, the fracture time is shorter, as shown in Tab. 4.3. Even though all three 10% side grooved specimens initial K_{max} values and test durations are different, the crack growth rate versus K_{max} slopes are all similar.

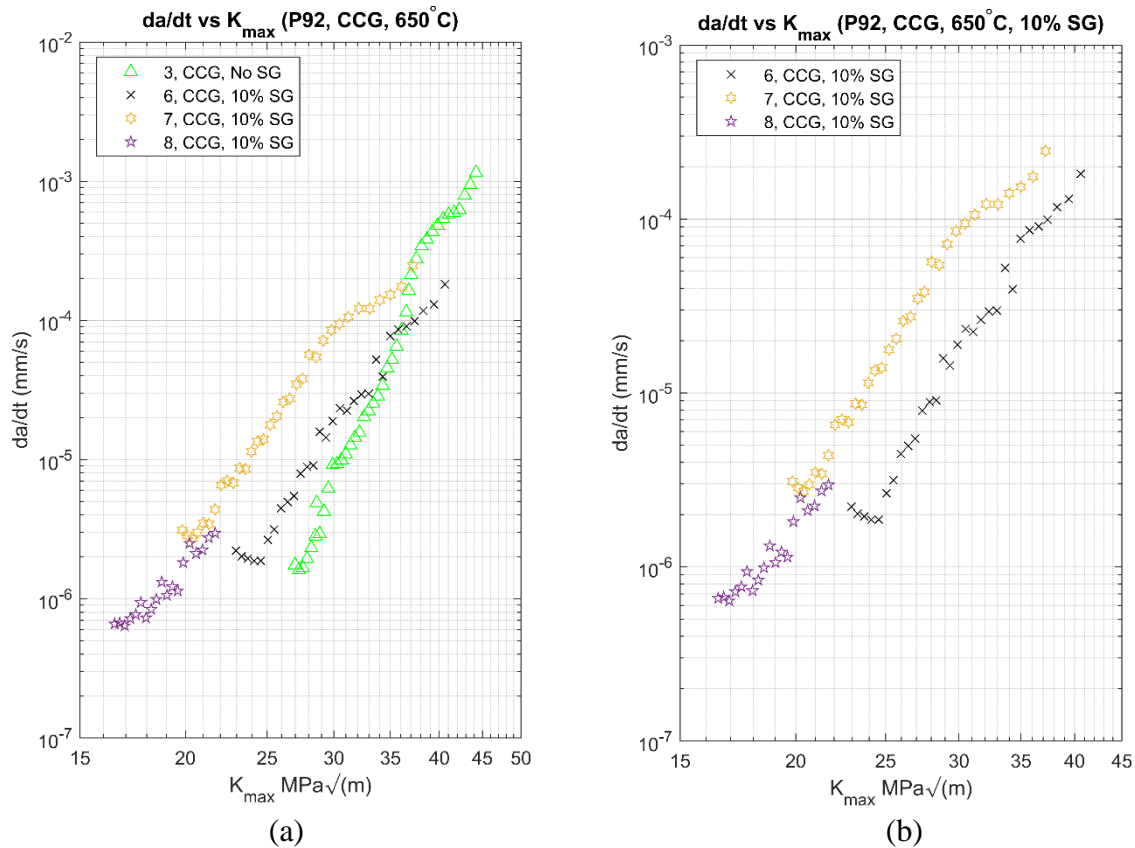


Fig. 4.6. (a) Graph of 10% and no side groove CCG specimens, (b) graph of just 10% side grooved CCG specimens.

Specimen 8 started at a much lower initial K_{max} value resulting in a lower crack growth rate per time. This test in particular is of high importance for this study. Specimen 8 achieved the 1000-hr plus goal, even though the test ended with about half the crack growth of the other tests. As well as all the crack growth data for the test correlates with specimen 6 and 7.

An additional comparison can be made using C^* which is a time dependent creep crack growth parameter. C^* , also called the contour integral, considers K with the addition of the load line displacement, and some material specific creep constants as shown in [3, eq. (2.10)]. Fig. 4.7 is a plot of time dependent crack growth rate, da/dt , versus the crack tip parameter, C^* . Note that da/dt is in mm/hr on this plot compared to mm/s for the da/dt versus K_{max} plot. When the three 10% side grooved CCG specimens are plotted as a function of C^* , the data from specimens 6 and 7 collapse on top of each other and those from specimen 8 are still within the same scatter band. The data for specimen 8 start at a lower K_{max} value which results in starting at a lower C^* value. C^* correlates the data of the CCG tests better than K_{max} as seen when comparing Fig. 4.6(b) with Fig. 4.7.

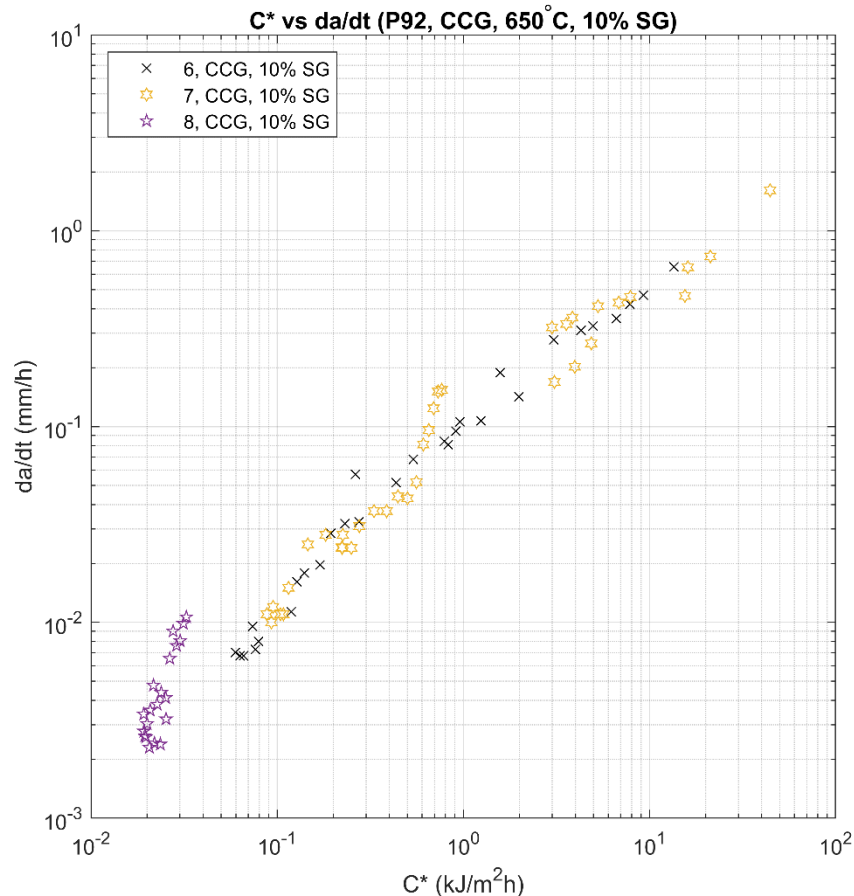


Fig. 4.7. Crack growth rate, da/dt , versus contour integral, C^* .

Fig. 4.8 compares the data reduced in this thesis to data collected by Tabuchi *et al.* as part of a round robin study [9]. Tabuchi *et al.* [9] performed P92 parent material experiments at 650°C. They used CT specimens, however there are some material and geometry differences compared to the specimens used in this study. The specimens used in the round robin were from a 30 mm thick plate with a heat treatment normalizing at 1050°C for two hrs and tempering at 780°C for two hrs. The round robin specimens had a notch size of 23.4 mm, a precrack of about 3 mm and a crack growth of 4 to 6 mm compared to the specimens in this study that have a notch size of about 10 mm, precrack of 8 mm and crack growth of 9 to 13 mm. All three CCG experiments conducted coalesce with the 650°C parent material tests conducted by this Tabuchi *et al.* [9]. All three CCG tests in this study show a higher da/dt value per C^* value compared to the round robin tests. At lower da/dt values on the graph in Fig. 4.8 show that the tests in this study grew roughly two times faster than the round robin tests. At higher crack growth rates, the difference is about five times faster.

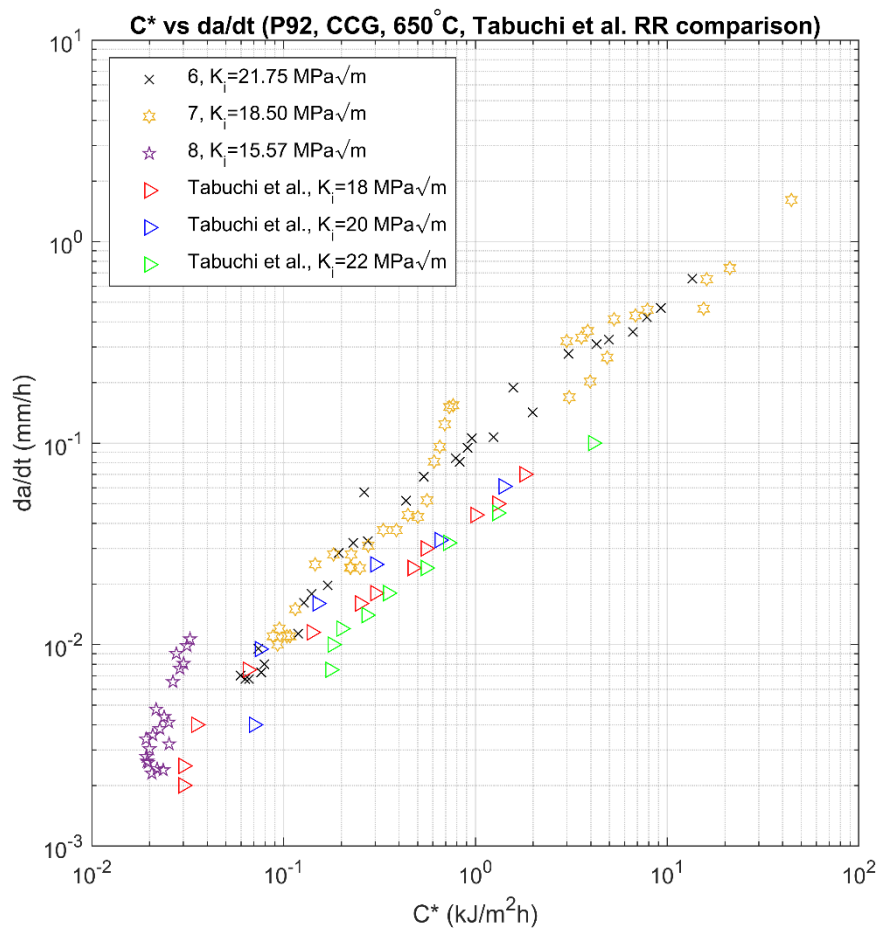


Fig. 4.8. Comparing Tabuchi *et al.* [9] round robin data with tests performed.

LLD for each of the 10% CCG specimens are plotted in Fig. 4.9(a). In general, most of the LLD occurs near the end of the CCG test. LLD rate can be broken down into three different sections: the total load line displacement rate (\dot{V} or ΔV rate), the creep portion of load line displacement rate (\dot{V}_c or ΔV_c rate), and the elastic portion of load line displacement rate (\dot{V}_e or ΔV_e rate). Fig. 4.9(b) shows how each of these load line displacement portions compare versus crack length for specimen 6, which is similar to specimen 7 and 8. The creep load line displacement rate portion consists of approximately 80% of the total load line displacement rate while the elastic portion consists of about 20% as shown in Fig. 4.9(b). For a material to be classified as creep ductile, this should be the case for the duration of the test.

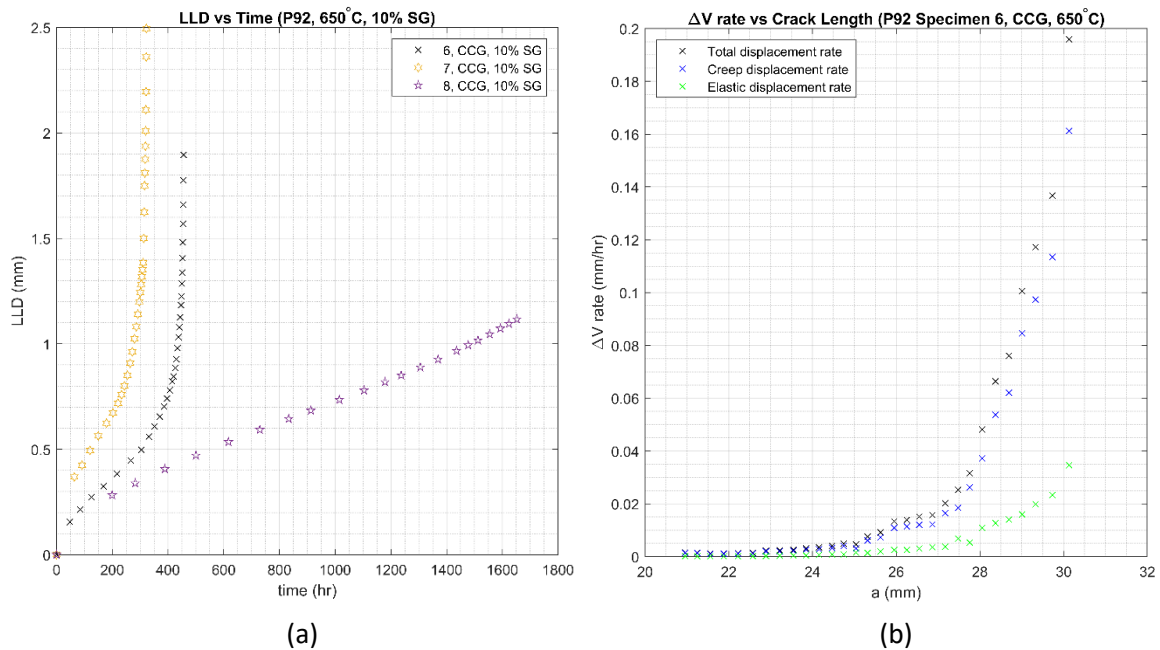


Fig. 4.9. (a) Load line displacement for 10% side grooved CCG tests. (b) Load line displacement breakdown for specimen 6.

There were two validity calculations conducted to see if the crack growth behavior acted in a creep brittle or creep ductile manner. These are LLD ratio and non-dimensional crack velocity, λ [5, eq. (4.4)]. The LLD ratio finds the percentage of LLD that is due to creep versus due to the elasticity. Non-dimensional crack velocity looks at how quickly the crack tip field changes as the crack propagates.

LLD ratio uses the creep load line displacement rate, \dot{V}_c , divided by the total LLD rate, \dot{V} , to see how much of the LLD is dominated by creep behavior. As the creep LLD rate of the total LLD rate increases, a material becomes more ductile. When the creep LLD rate becomes greater than the elastic LLD rate, the material can be characterized as a creep ductile material. For values of $\dot{V}_c/\dot{V} > 0.5$ the material's LLD is dominated by the creep portion and should be classified as a creep ductile material, and the crack growth should be characterized with the contour integral, C^* . For values of $\dot{V}_c/\dot{V} < 0.5$ the material's LLD is dominated by the elastic portion and should be classified as a creep brittle material, and the crack growth should be characterized with the stress intensity factor, K [3]. As seen in Tab. 4.2, the LLD ratios for specimens 6, 7, and 8 are greater than 0.5 and therefore show creep ductile behavior, leading to characterization using the C^* parameter.

Non-dimensional crack velocity is defined by [5, eq. (4.4)],

$$\lambda = \frac{\dot{a} \sigma_{ref}^2 (1 - \nu^2)}{EC^*} \quad (4.4)$$

where \dot{a} is the crack growth rate, σ_{ref} is the reference stress, E is the material modulus of elasticity, and ν is Poisson's ratio. Reference stress is calculated as the mean of plane strain reference stress, $\sigma_{refPL\epsilon}$, and plane stress reference stress, $\sigma_{refPL\sigma}$. These are calculated using [11, eq. (4.5) and (4.6)] with the initial reference stress values for specimens 6, 7, and 8 shown in Tab. 4.4.

$$\sigma_{refPL\epsilon} = \frac{P}{BW} \frac{1}{-\frac{2}{\sqrt{3}} \left(1 + 1.702 \left(\frac{a}{W}\right)\right) + \frac{2}{\sqrt{3}} \left(2.702 + 4.599 \left(\frac{a}{W}\right)^2\right)^{\frac{1}{2}}} \quad (4.5)$$

When non-dimensional crack velocity is greater than one, $\lambda \gg 1$, elastic effects are

$$\sigma_{refPL\sigma} = \frac{P}{BW} \frac{1}{-\left(1 + \frac{2}{\sqrt{3}} \left(\frac{a}{W}\right)\right) + \left(\left(1 + \frac{2}{\sqrt{3}}\right) \left(1 + \frac{2}{\sqrt{3}} \left(\frac{a}{W}\right)^2\right)\right)^{\frac{1}{2}}} \quad (4.6)$$

dominant [5] and the crack tip parameter should be characterized using the stress intensity factor, K . This is when the crack is growing relatively quick compared to the creep damage forming. If the non-dimensional crack velocity is less than one, $\lambda \ll 1$, creep effects are

dominant and the contour integral, C^* , should be used to characterize the crack tip parameter. This validity check coincides with what the LLD ratio recommends: C^* should be used to characterize the crack tip parameter for CCG tests conducted since the crack tip is dominated by creep effects. Thus, this validity check confirms that this specific heat of P92 shows creep ductile behavior.

Tab. 4.4. Calculated values for specimen 6, 7, and 8.

Test	Specimen 6	Specimen 7	Specimen 8
Initial reference stress (MPa)	80.63	66.63	54.73
Non-dimensional crack velocity	0.0107	0.0037	0.0013
Load line displacement ratio	0.8274	0.8780	0.8818

4.6 Fractography

Half of a CT specimen from three different CCG tests (6, 7, and 8) were sent to EPRI to be sectioned using EDM. Specimens 6 and 7 were sectioned down the mid plane and a single, mounted, polished sample from each test was sent back to analyze. Specimen 8 was sectioned at three points through the thickness of the specimen and is described in more detail in Section 4.6.3. These sectioned samples allow the material to be analyzed below the fracture surface which is covered by an oxide layer. Items of interest below the fracture surface include boron nitride (BN) inclusions, creep voids/cavities, and secondary cracking or tunneling.

4.6.1 EDS

To confirm that there was an oxide layer on top of the fracture surface, an energy dispersive X-ray spectrometer (EDS) attachment was used to verify the material composition of the theoretical oxide layer and the underlying raw material. Fig. 4.10(a) and 4.11(a) show where the EDS was used on the subsurface material and the corresponding raw material composition for that point. Fig. 4.10(b) and 4.11(b) show where the EDS was positioned for proof of the oxide layer and the corresponding oxide layer material composition, respectively.

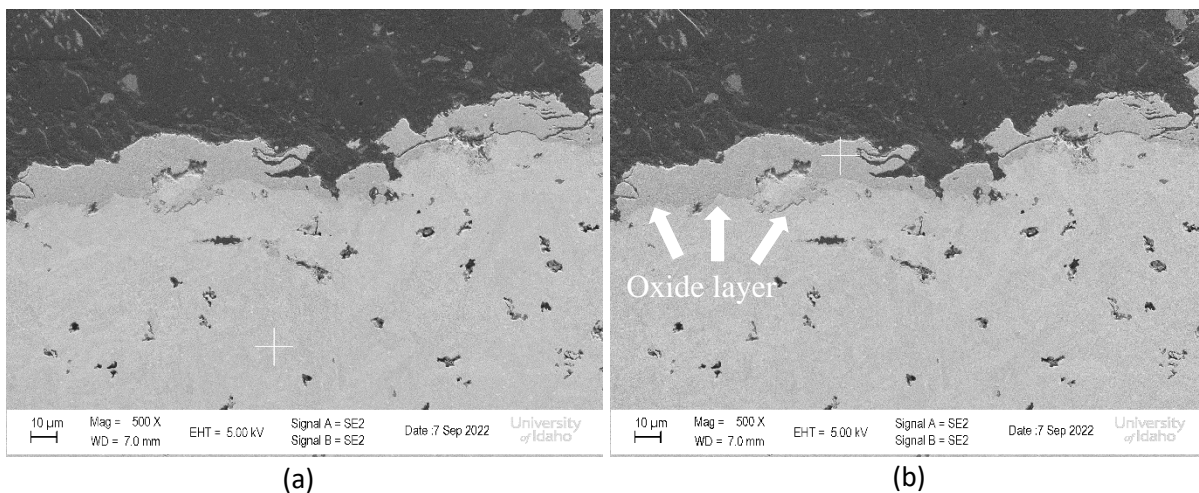


Fig. 4.10. (a) EDS spot used for material composition, (b) EDS spot used for oxidation layer.

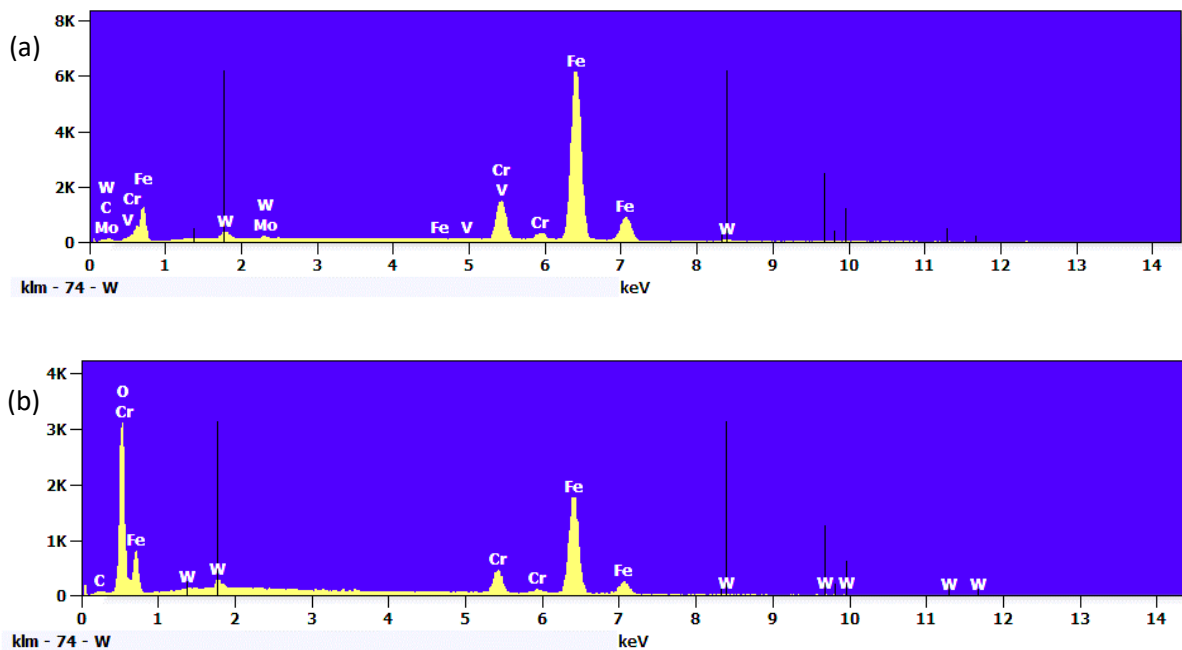


Fig. 4.11. (a) EDS material reading for Fig. 4.10(a), (b) EDS material reading for Fig. 4.10(b).

The oxide layer shows up as a darker gray for all the SEM images in this study as shown in Fig. 4.10.

All commercial P92 is expected to have boron nitride (BN) [10] inclusions. Fig. 4.12 shows two creep cavities that were scanned using EDS to identify material composition. As shown in Fig. 4.13, BN was identified within both cavities. Cavities that develop from BN often grow in a faceted way, as seen in Fig. 4.12(b), compared to the typical elongated oval cavity in the crack growth direction. These inclusions are undesirable for creep resistance in materials.

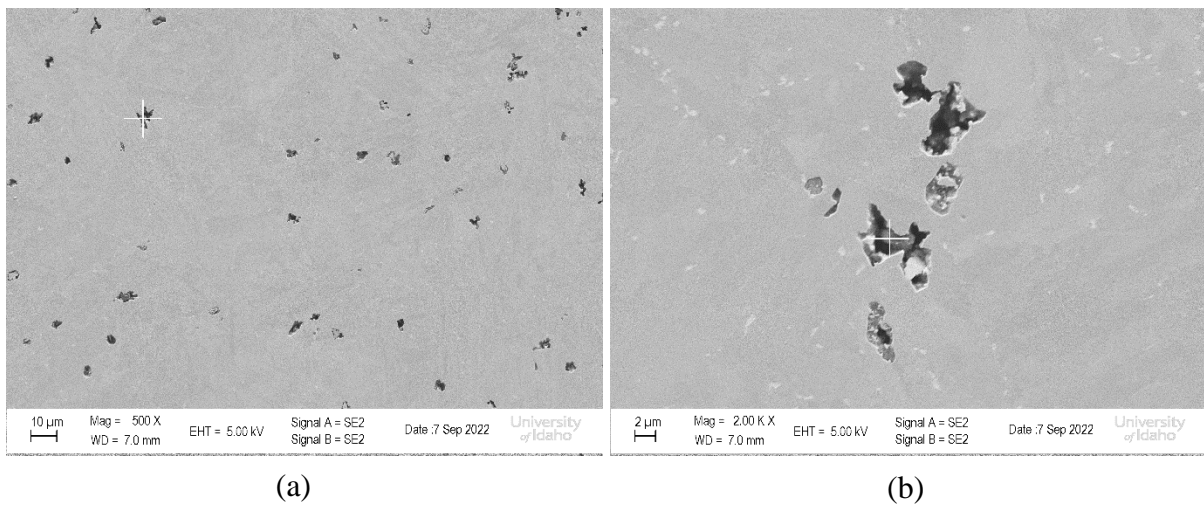


Fig. 4.12. Points EDS was used to see BN inclusions.

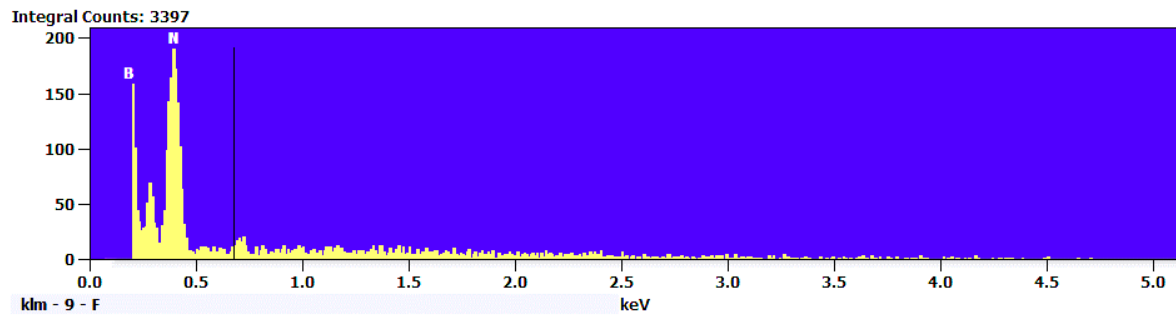


Fig. 4.13. EDS material reading for BN spots in Fig. 4.12.

4.6.2 Creep Voids and Secondary Cracking

Fig. 4.14(a) (b) and (c) show SEM images of specimens 6, 7, and 8, respectively, indicating the structures directly below the fracture surface. All three images were taken at the same magnification and same settings in the SEM. Specimen 8 was of particular interest due to the number of voids below the surface and the test duration of greater than 1000 hrs. Both

specimens 6 and 7 overall showed fewer voids and creep cavities below the fracture surface compared to specimen 8. This is attributed to specimen's 6 and 7 having a test duration of less than 500 hrs while specimen 8's test duration was greater than 1700 hrs. As the life of a given CCG test increased, the void density increased. This can be observed especially in specimen 8 where the CCG life was approximately four times greater than specimens 6 and 7. The void density increase observed in specimen 8 is attributed to the time the specimen was exposed to the sustained creep load, thus, more time was available to develop creep strain at the tip of the crack leading to more extensive void formation.

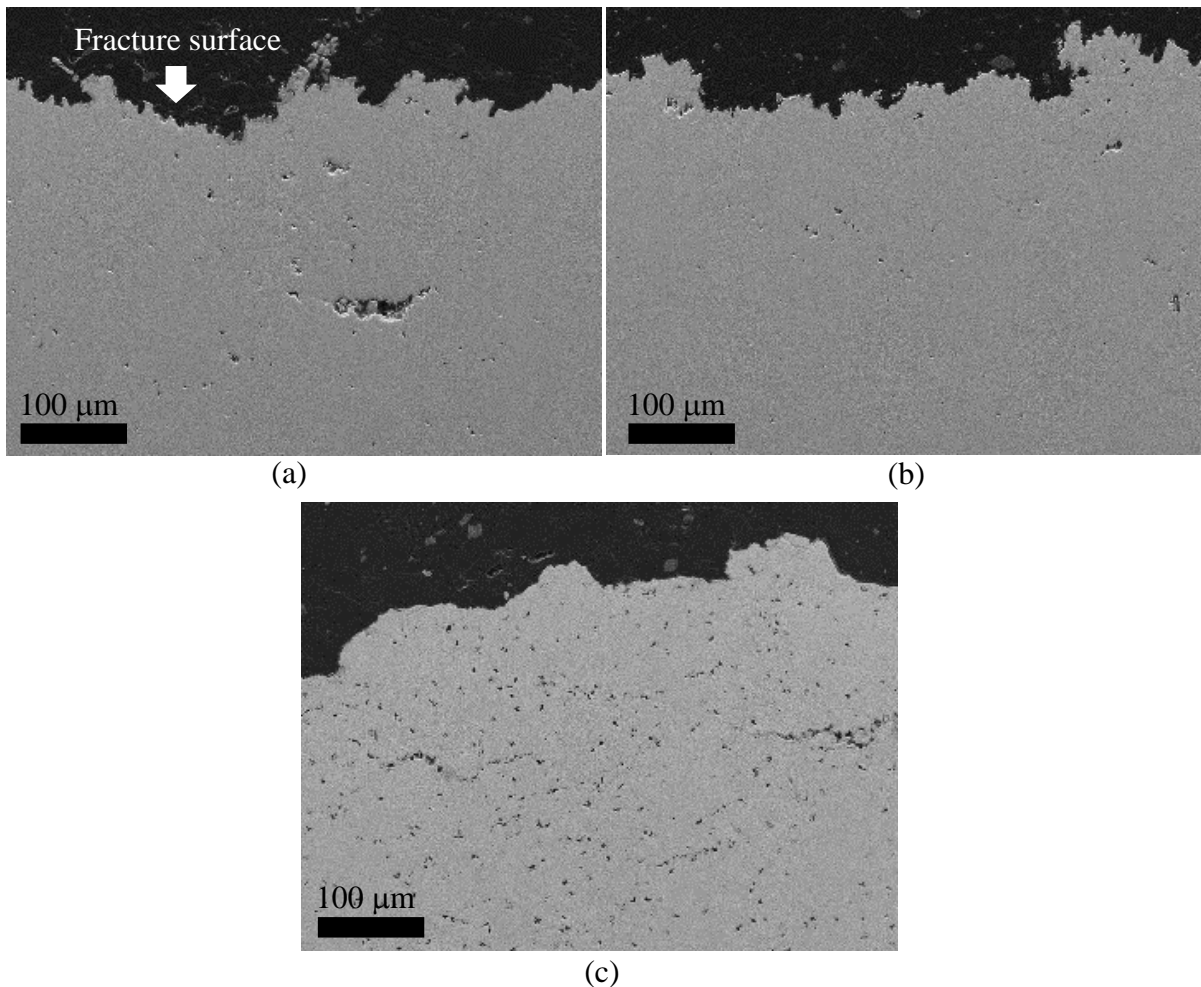


Fig. 4.14. (a) Specimen 6, (b) Specimen 7, (c) Specimen 8.

Secondary cracking was observed on the fracture surfaces. These secondary cracks on the fracture surfaces are pointed out by yellow arrows in Fig. 4.15. However, all of these secondary cracks extend beyond the typical CCG crack region and into the post-test cyclic area. To confirm that there was secondary cracking in the CCG region, oxide layers around creep voids and cavities were searched for in the sectioned samples. Oxidation occurs when the material is subjected to oxygen in the heated environment. Therefore, the cavities below the fracture surfaces that have an oxide layer around them are secondary cracks that formed from the coalescence of creep voids from the main, primary crack. Each specimen showed creep voids and sections of these creep voids starting to coalesce and form secondary cracking. Fig. 4.16 shows an oxidation layer below the fracture surface along the creep cavities that became a secondary crack. This image was taken in the CCG region implying that secondary cracking occurred throughout the duration of the test.

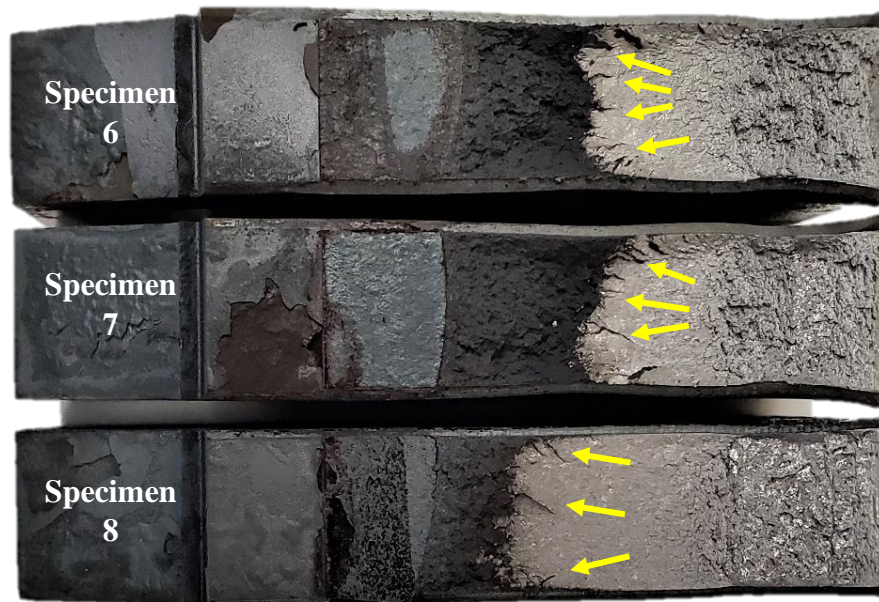


Fig. 4.15. Specimen 6, 7, and 8 fracture surface.

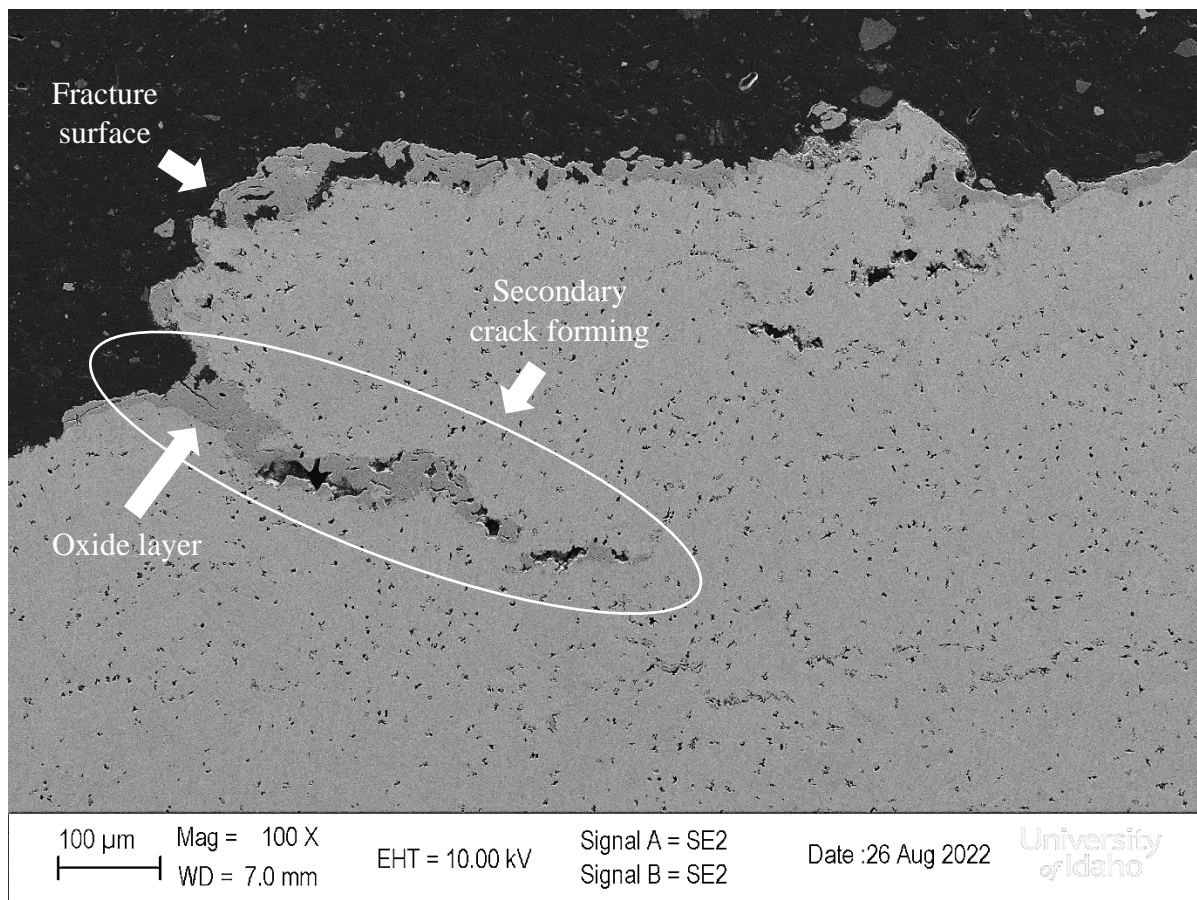


Fig. 4.16. Example of secondary cracking seen below the fracture surface.

4.6.3 Specimen 8 Void Density Analysis

EPRI sectioned specimen 8 into three sections as shown in Fig. 4.17: one at the mid plane of the specimen, one at the 1/4 plane, and one at the 1/8 plane of the specimen. An optical image of each plane is shown in Fig. 4.18. This specimen was sectioned so that the area below the fracture surface could be analyzed for all three sections and compared to each other. This allowed for a comparison of the creep behavior throughout the test at different locations along

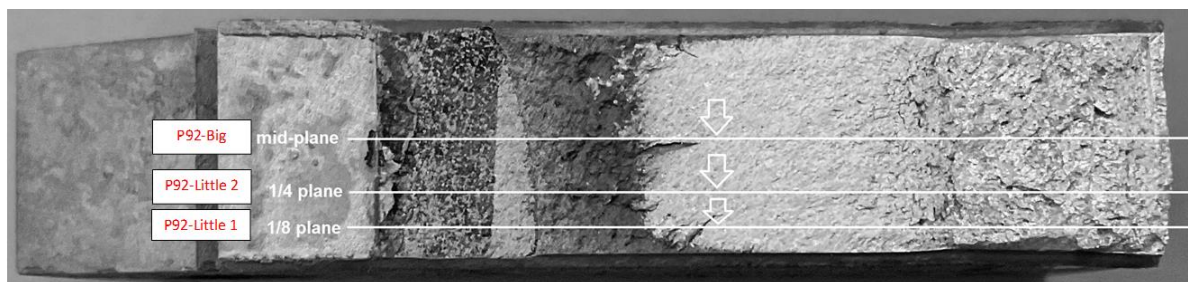


Fig. 4.17. Image from EPRI of where each plane was sectioned. [10]

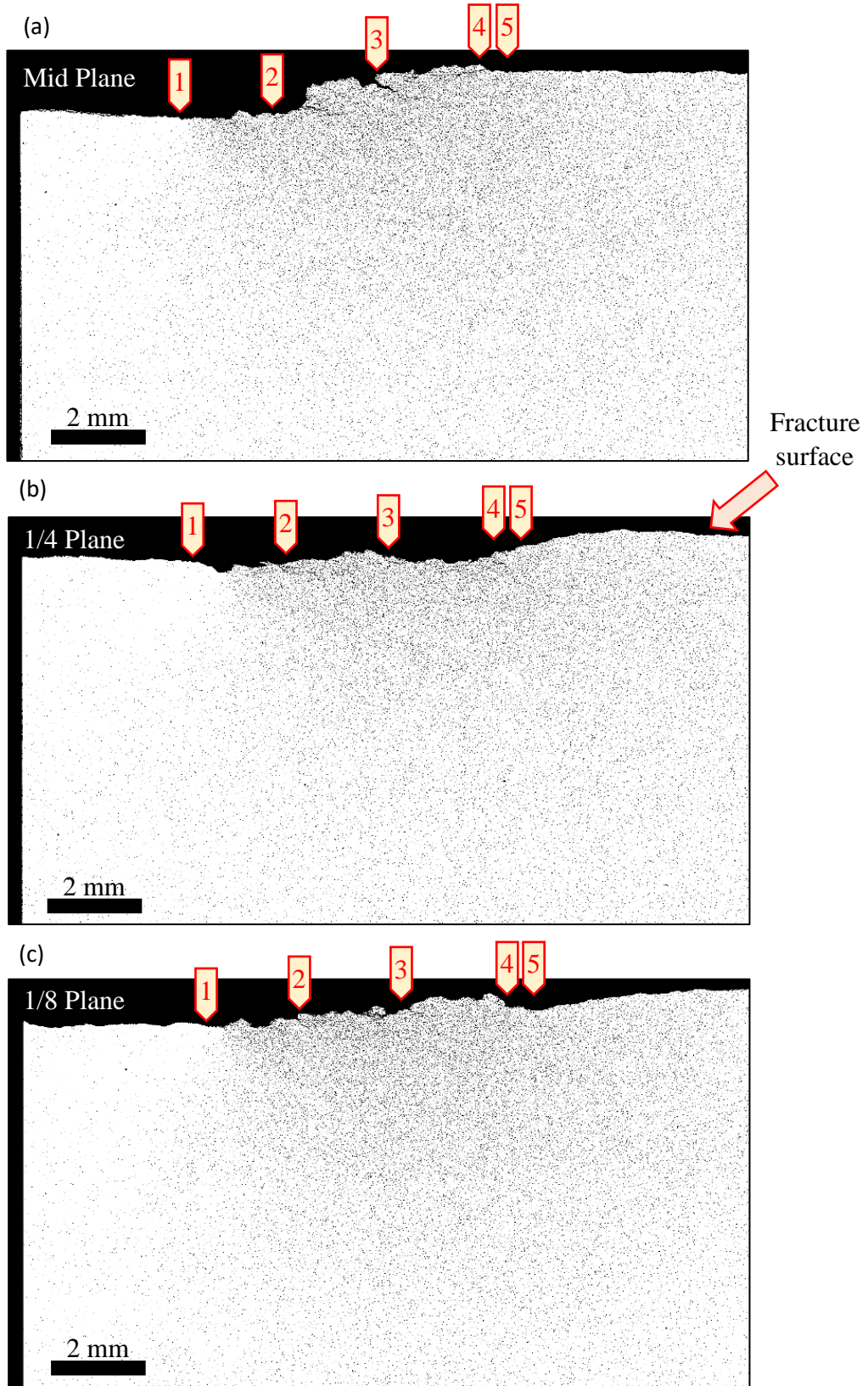


Fig. 4.18. Optical images of each plane of specimen 8 with points marked where void density analyses was conducted.

the specimen thickness. Under steady state creep the uncracked ligament of the specimen is dominated by creep deformation. Point number five in Fig. 4.18 is the final crack length of the test labeled on each section (mid, 1/4 and 1/8). Since there is creep deformation to the right of point five (ahead of the final crack length tip) in each image, the images show that each section of specimen 8 was in steady state creep.

A void density analysis was performed on each of these specimen planes with the results shown quantitatively in Appendix C.1 and graphically in Fig. 4.19. At the five points referenced in Tab. 4.5 and Fig. 4.18, an image was taken at 0.5 mm, 1.0 mm, and 1.5 mm below the fracture surface at 400x magnification. To maintain consistency, every void was counted in each area analyzed below the fracture surface.

Tab. 4.5. Locations at which void density analyses were conducted.

Marker #	a (mm)	t (hr)	K_{max} (MPa \sqrt{m})
1	17.46	0	15.57
2	19.46	635	17.24
3	21.46	1270	19.14
4	23.46	1600	21.37
5	23.88	1734	21.88

The left three graphs in Fig. 4.19 show a consistent density for each of the three sections (mid, 1/4 and 1/8) at a certain distance below the fracture surface. These three plots also show that the average void density decreases by approximately 13% from 0.5 mm below the fracture surface to 1.0 mm below the fracture surface. From 1.0 mm to 1.5 mm below the fracture surface the average void density decreases by approximately 20%. This shows that the void density progressively decreases as the creep deformation is analyzed the further away from the crack front.

The right three graphs in Fig. 4.19 show the difference in void density for an individual specimen plane at the three distances below the fracture surface. These three graphs show that at a distance further away from the crack front (below the surface) the void density decreases per plane (mid, 1/4, 1/8 plane) just as the left three graphs showed. The mid, 1/4 and 1/8 plane graphs show that the 1/8 plane has the least variance of void density as the sample is analyzed going below the crack front. This implies that the change in void density from one depth below

the crack front to the next is more consistent, i.e., 12% decrease from 0.5 mm to 1.0 mm and 10% decrease from 1.0 mm to 1.5 mm.

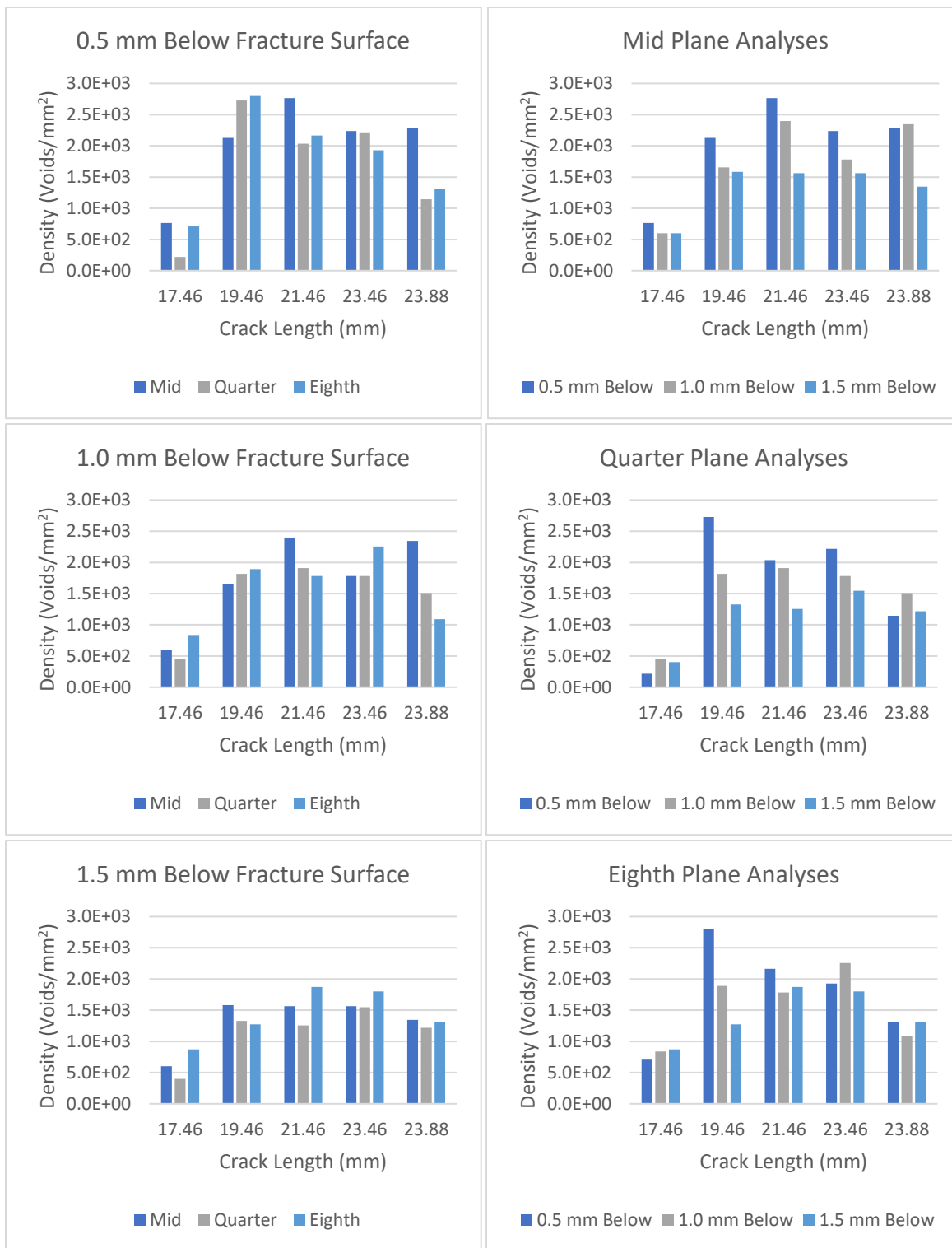


Fig. 4.19. Left three graphs are comparing a specific distance below the fracture surface per graph for each plane. Right three graphs are comparing each plane per graph at different distances below the crack front.

5. CONCLUSIONS AND RECOMMENDATIONS

5.1 Conclusions

There were three different side groove percentages explored in this study on the CT specimens. Specimens without side grooves exhibited significant crack tunneling. A 20% side groove resulted in the opposite effect with the crack front propagating quicker on the sides of the specimen and slower in the center. 10% side grooves resulted in the most uniform crack front propagation. Since this percentage of side grooves proved to have the most uniform crack front propagation the rest of the tests performed had 10% total side grooves added to the specimens.

Three creep fatigue crack growth (CFCG) tests were performed under the same testing conditions with the three different side groove percentages. These three tests correlate within the same scatter band on a crack growth rate per cycle, da/dN , versus stress intensity factor, ΔK , plot. However, when the data are plotted with respect to crack growth rate per time, da/dt , versus stress intensity factor, K_{max} , specimen 9's data tails off with a slower crack growth rate at the end of the test. These three specimens were then plotted with respect to crack growth rate per time, da/dt , versus the contour integral, $(C_t)_{avg}$ to consider the creep load line displacement (LLD) portion. On this plot, the data for the three specimens' collapse on top of each other. For CFCG tests $(C_t)_{avg}$ should be used to characterize crack tip growth rather than the stress intensity factor since it takes into account the creep LLD deformation, ΔV_c , the stress intensity factor, K , and some additional material constants.

The creep crack growth (CCG) tests performed all started at a different initial K_{max} value. The slopes of these data sets are all similar to each other. These CCG tests were also correlated to each other using the contour integral, C^* . Each data set for the three 10% side grooved specimens fall on top of each other when plotted as crack growth rate per time, da/dt , versus crack tip parameter, C^* . Specimen 8 started at the lowest K_{max} value of all the tests performed and was not completed due to a power outage so only low CCG rate data were generated from the test. If the specimen had been tested to failure, the additional crack growth data would be expected to follow the data for specimens 6 and 7. These three tests were compared to the Japanese round robin data for the parent material tested at 650°C. All three tests performed in

this study showed a higher crack growth rate (two to five times faster) than the Japanese results for a given C^* value.

Two validity checks were performed to determine if the CCG tests conducted on P92 in this study behaved in a creep brittle or creep ductile manner. The non-dimensional crack velocity values were less than one for all three specimens meaning that the crack growth rate was relatively slow compared to the creep deformation occurring. This implies that the CCG tests behaved in a creep ductile manner and should be correlated using the contour integral, C^* , rather than the stress intensity factor, K . The second creep ductile versus creep brittle validity check calculated was the LLD ratio. All three specimens had LLD ratios greater than 0.5 which corresponds to a creep ductile manner and C^* should be used as the crack tip parameter. Therefore, based on the findings in this research and the validity checks, P92 behaved in a creep ductile manner compared to a creep brittle manner.

Creep crack growth specimens 6, 7 and 8 were sectioned, mounted, and analyzed. BN inclusions were found in creep voids using an EDS attachment on an SEM and is consistent with commercial P92. These inclusions grew in a faceted fashion. Oxidation layers were found on the fracture surface and below the surface around voids. These oxidation layers around voids show that there is secondary cracking happening and that these voids are coalescing to form this secondary crack which connects to the fracture surface somewhere through the thickness of the specimen. As the CCG life for a given test increase, the void density increased. The void density increase with CCG life allowed more creep strain to develop at the tip of the crack and surrounding affected material.

Specimen 8 was sectioned into three different planes for a comparative analysis between each plane. The 1/8 plane was found to have the most consistent void density between the three distances below the crack front. All three planes showed a trend of the void density decreasing as the creep deformation gets further away from the fracture surface.

5.2 Recommendations

All tests conducted in this study used parent material P92. These can be compared to a new component in a power plant being tested. However, performing similar tests with aged material to see if the behavior around the crack tip is the same or different than the parent

material would be of interest. An aged material is a material that has been subjected to similar environmental conditions as the components used in the application. For this research study, the application and conditions would be components in thermal power plants with temperatures around 600°C. Performing tests on aged material would help characterize how the material's creep deformation and crack growth behaves for a component that has been in service. The specimens should be aged for the same duration that the component would be in service if possible or an equivalent aging process to create the aged condition desired.

Performing a test that is similar to specimen 8 (CCG test with a test time duration greater than 1000 hrs) except interrupted at certain time increments within the test could be conducted. By doing this, the creep damage that occurs at different stages of a test can be analyzed especially around the crack tip. To do this, the specimen should not be ripped apart into two halves like the tests in this study. Instead, the test should be stopped, and the specimen removed still intact to be machined, polished, and mounted as is.

A CCG test that begins at a lower K_{max} than specimen 8 is recommended. This test should result in a longer life since it will start at a lower stress intensity value. Since specimen 8's test ran for 1700 hrs it was exposed to high temperature and oxidation for a relatively long time period. A longer life test would be of interest to compare to specimen 8 to see how unique or equivalent the creep deformation is when exposed to these extreme conditions. Although time invested in creep crack growth studies is significant, attempting to simulate real time conditions is critical in evaluating the actual damage mechanisms in P92 components. A longer CCG test would help simulate these real time conditions.

Only creep fatigue crack growth tests with 60 s hold times were conducted in this study. Creep fatigue crack growth tests with various hold times, i.e., 6 s, 600 s, etc. could be evaluated to see how this parent material behaves under various hold time conditions.

A more detailed material characterization analysis regarding the creep damage around the crack tip should be conducted to determine the material constituent contributions to the creep and crack growth behavior. In addition, void density analysis in this study was conducted manually. It would be recommended to incorporate a more consistent density analysis technique, i.e., an image recognition software.

6. REFERENCES

- [1] A. Saxena, *Nonlinear Fracture Mechanics for Engineers*, Boca Raton: CRC Press, 1998.
- [2] R. I. Stephens, A. Fatemi, R. R. Stephens and H. O. Fuchs, *Metal Fatigue in Engineering*, New York: John Wiley & Sons Inc., 2000.
- [3] ASTM E1457-98, *Test Method for Measurement of Creep Crack Growth Rates in Metals*, ASTM International, West Conshohocken, PA, 1999.
- [4] M. F. Ashby and D. R. H. Jones, *Engineering Materials 1 an Introduction to their Properties & Applications*, Oxford: Butterworth-Heinemann, 1996.
- [5] G. A. Webster and R. A. Ainsworth, *High Temperature Component Life Assessment*, London: Chapman & Hall, 1994.
- [6] ASTM E2760-19e1, *Standard Test Method for Creep-Fatigue Crack Growth Testing*, ASTM International, West Conshohocken, PA, 2019.
- [7] M. Saber, "Experimental and Finite Element Studies of Creep and Creep Crack Growth in P91 and P92 Weldments," Nottingham, 2011.
- [8] A. T. Yokobori Jr., "Difference in the creep and creep crack growth behavior between creep ductile and creep brittle materials," *Engineering Fracture Mechanics*, vol. 62, no. 1, pp. 61-78, 1999.
- [9] M. Tabuchi, A. T. Yokobori Jr., R. Sugiura, M. Yatomi and A. Fuji, K. Kobayashi, "Results of a Japanese round robin program for creep crack growth using Gr. 92 steel welds," *Engineering Fracture Mechanics*, vol. 77, no. 15, pp. 3066-3076, 2010.
- [10] Electrical Power Research Institute, "Background for Heat 6292921," Charlotte, NC, 2022.
- [11] I. Perrin, "Review of Grade 92 Creep Crack Growth Tests," Charlotte, NC, 2022.
- [12] ASTM E647-95a, *Test Method for Measurement of Fatigue Crack Growth Rates*, ASTM International, West Conshohocken, PA, 1999.
- [13] K. Schwalbe and J. Landes, "An analysis of creep deformation parameters. Part 1: background," *Engineering Fracture Mechanics*, vol. 71, no. 16-17, pp. 2449-2461, 2004.
- [14] C. Gibson, R. Stephens, S. B. Narasimhachary, D. E. Mills, and A. Rosenberger, "Results of a Pilot Study in Support of a Round-Robin on Creep-Fatigue Crack Growth Testing of a Creep-Brittle Material for ASTM E2760," *Materials Performance and characterization*, vol. 11, no. 1, 2022.
- [15] V. Viswanathan, R. Purgert and P. Rawls, "Coal-Fired Power Materials", 2008.

- [16] “Power Generation from Coal Soaring in 2021,” IER, Oct. 18, 2021.
<http://www.instituteforenergyresearch.org/fossil-fuels/coal/power-generation-from-coal-soaring-in-2021/> (accessed Oct. 12, 2022).
- [17] POWER, “AEP’s John W. Turk, Jr. Power Plant Earns POWER’s Highest Honor,” POWER Magazine, Aug. 01, 2013. <https://www.powermag.com/aeps-john-w-turk-jr-power-plant-earns-powers-highest-honor/> (accessed Oct. 14, 2022).
- [18] ASTM E21-92, Standard Test Methods for Elevated Temperature Tension Tests of Metallic Materials, ASTM International, West Conshohocken, PA, 1999.

7. APPENDICES

Appendix A. Raw Test Data

A.1 P92-1 (15 Hz)

Fatigue Crack Growth, 15 Hz, 650°C		
a (mm)	cycles	t (hr)
18.40	0	0
19.79	5222	0.09
20.15	7043	0.12
20.50	8814	0.15
20.85	10570	0.19
21.21	12208	0.21
21.56	13892	0.24
21.90	15487	0.27
22.25	17029	0.30
22.58	18431	0.32
22.92	19898	0.35
23.24	21263	0.37
23.58	22608	0.40
23.91	23825	0.42
24.24	24942	0.44
24.58	26110	0.46
24.92	27203	0.48
25.27	28297	0.50
25.63	29438	0.52
25.98	30516	0.54
26.32	31464	0.55
26.66	32427	0.57
26.99	33268	0.58
27.32	34105	0.60
27.64	34922	0.61
27.96	35628	0.63
28.28	36309	0.64
28.60	36979	0.65
28.93	37585	0.66
29.26	38154	0.67
29.62	38744	0.68
29.99	39249	0.69
30.35	39752	0.70

30.71	40227	0.71
31.08	40664	0.71
31.45	41108	0.72
31.82	41514	0.73
32.18	41843	0.73

A.2 P92-2

Creep Fatigue Crack Growth, 60 sec, 650°C		
a (mm)	cycles	t (hr)
19.28	0	0
20.23	1202	20.12
20.46	1637	27.39
20.69	2099	35.12
20.93	2566	42.94
21.16	3028	50.67
21.41	3484	58.30
21.64	3939	65.91
21.87	4399	73.61
22.10	4822	80.69
22.33	5257	87.96
22.56	5637	94.32
22.78	6005	100.49
23.00	6316	105.69
23.24	6647	111.23
23.49	6932	116.00
23.74	7227	120.93
23.99	7487	125.29
24.25	7741	129.53
24.51	7974	133.44
24.78	8216	137.49
25.04	8439	141.22
25.30	8674	145.14
25.56	8858	148.22
25.82	9023	150.98
26.07	9174	153.51
26.33	9311	155.81
26.56	9430	157.80
26.81	9525	159.39

27.05	9600	160.65
27.29	9667	161.77
27.52	9726	162.75
27.77	9779	163.63
28.03	9822	164.36
28.28	9858	164.96
28.54	9886	165.43
28.80	9909	165.81
29.08	9929	166.14
29.36	9943	166.38
29.63	9954	166.57

A.3 P92-3

Creep Crack Growth, 650°C		
a (mm)	t (hr)	LLD (mm)
19.20	0	0
19.99	90.43	0.284794
20.19	123.41	0.3851
20.40	159.22	0.487331
20.61	194.13	0.591537
20.82	224.36	0.698835
21.04	250.29	0.810873
21.25	271.64	0.925007
21.47	292.20	1.041202
21.69	306.58	1.160473
21.91	316.42	1.281501
22.13	323.22	1.407254
22.35	329.82	1.533418
22.57	335.96	1.660571
22.79	341.51	1.788669
23.01	346.32	1.920255
23.23	350.54	2.052871
23.45	354.49	2.189585
23.67	357.48	2.325884
23.89	360.20	2.463953
24.11	362.55	2.601983
24.33	364.70	2.745475
24.54	366.49	2.889341

24.76	367.82	3.034591
24.98	368.96	3.180497
25.19	369.88	3.327615
25.41	370.59	3.47659
25.63	371.11	3.629673
25.84	371.40	3.783641
26.07	371.62	3.944806
26.30	371.81	4.112605
26.53	371.97	4.281824
26.75	372.12	4.452917
26.98	372.25	4.626482
27.21	372.37	4.800259
27.44	372.48	4.976294
27.66	372.59	5.150318
27.88	372.68	5.321559
28.09	372.76	5.495383
28.31	372.82	5.672202

A.4 P92-4

Creep Fatigue Crack Growth, 60 sec, 650°C		
a (mm)	cycles	t (hr)
18.08	0	0
18.97	1321	22.16
19.20	1807	30.33
19.42	2348	39.39
19.65	2859	47.97
19.88	3394	56.95
20.12	3953	66.33
20.37	4515	75.76
20.60	5088	85.38
20.83	5608	94.10
21.05	6096	102.29
21.28	6539	109.73
21.50	6959	116.77
21.71	7354	123.40
21.92	7701	129.23
22.13	8037	134.86
22.35	8350	140.11

22.56	8648	145.13
22.78	8963	150.40
23.01	9228	154.85
23.24	9489	159.22
23.47	9734	163.35
23.70	9939	166.79
23.93	10134	170.05
24.15	10308	172.97
24.37	10448	175.32
24.58	10582	177.57
24.80	10699	179.53
25.01	10809	181.38
25.23	10929	183.39
25.44	11041	185.27
25.66	11148	187.08
25.87	11253	188.83
26.09	11357	190.57
26.30	11454	192.20
26.53	11547	193.76
26.74	11631	195.18
26.96	11706	196.43
27.17	11772	197.53
27.39	11832	198.54
27.61	11884	199.42
27.83	11931	200.21
28.05	11972	200.90
28.27	12008	201.49
28.49	12038	202.00
28.71	12064	202.43
28.93	12085	202.79
29.15	12104	203.11
29.38	12118	203.35
29.61	12131	203.56
29.85	12138	203.68
30.10	12144	203.79
30.36	12149	203.87
30.62	12153	203.94
30.88	12157	204.00

A.5 P92-6

Creep Crack Growth, 650°C		
a (mm)	t (hr)	LLD (mm)
19.64	0	0
20.66	48.01	0.16
20.96	85.05	0.21
21.25	125.14	0.27
21.56	168.97	0.32
21.88	217.17	0.38
22.22	266.93	0.45
22.57	304.13	0.50
22.89	331.82	0.56
23.22	352.29	0.61
23.54	370.54	0.65
23.85	385.99	0.70
24.16	396.86	0.74
24.47	406.59	0.78
24.75	415.08	0.82
25.04	420.24	0.85
25.32	425.59	0.89
25.63	430.15	0.93
25.95	434.01	0.98
26.26	437.76	1.03
26.55	440.90	1.08
26.87	443.87	1.13
27.17	446.72	1.18
27.48	448.36	1.23
27.76	450.29	1.29
28.05	451.37	1.34
28.37	452.39	1.41
28.70	453.38	1.48
29.01	454.26	1.57
29.33	455.03	1.66
29.73	455.88	1.78
30.13	456.49	1.90

A.6 P92-7

Creep Crack Growth, 650°C		
a (mm)	t (hr)	LLD (mm)
18.54	0	0
20.09	63.87	0.37
20.39	91.57	0.42
20.71	120.26	0.49
21.02	149.85	0.56
21.32	179.16	0.62
21.60	202.40	0.67
21.87	220.61	0.72
22.18	233.20	0.76
22.48	243.94	0.80
22.77	254.47	0.85
23.07	264.20	0.91
23.36	272.05	0.96
23.64	279.79	1.02
23.92	286.00	1.08
24.17	291.89	1.14
24.44	297.11	1.20
24.73	300.64	1.24
25.03	303.73	1.28
25.36	306.38	1.32
25.70	308.68	1.35
26.06	310.98	1.38
26.39	312.97	1.50
26.74	314.67	1.63
27.11	316.07	1.75
27.47	317.18	1.81
27.81	318.19	1.88
28.14	319.11	1.94
28.46	319.90	2.01
28.80	320.64	2.11
29.12	321.38	2.20
29.41	322.01	2.36
29.75	322.52	2.50
30.06	322.95	2.64
30.46	323.20	2.82

A.7 P92-8

Creep Crack Growth, 650°C		
a (mm)	t (hr)	LLD (mm)
17.46	0	0
18.35	199.56	0.28
18.62	282.29	0.34
18.87	388.74	0.41
19.14	500.30	0.47
19.41	617.08	0.53
19.70	729.45	0.59
19.99	833.24	0.64
20.26	913.03	0.68
20.53	1015.03	0.73
20.80	1103.49	0.78
21.07	1178.81	0.82
21.34	1236.91	0.85
21.61	1305.78	0.89
21.88	1369.16	0.93
22.16	1435.48	0.97
22.43	1477.31	0.99
22.75	1512.47	1.02
23.07	1554.75	1.05
23.38	1592.99	1.07
23.68	1623.65	1.10
23.98	1652.18	1.12

A.8 P92-9

Creep Fatigue Crack Growth, 60 sec, 650°C		
a (mm)	cycles	t (hr)
18.60	0	0
19.75	122	2.06
20.02	250	4.21
20.29	535	9.00
20.56	939	15.80

20.83	1422	23.93
21.10	1956	32.92
21.38	2517	42.37
21.65	3088	51.97
21.92	3654	61.49
22.19	4205	70.77
22.46	4734	79.68
22.73	5238	88.16
23.01	5715	96.18
23.28	6163	103.72
23.55	6583	110.80
23.82	6978	117.44
24.09	7349	123.69
24.36	7699	129.58
24.63	8030	135.15
24.91	8344	140.43
25.18	8642	145.45
25.45	8926	150.23
25.72	9197	154.78
25.99	9453	159.10
26.26	9695	163.17
26.53	9922	166.98
26.81	10131	170.50
27.08	10321	173.70
27.35	10491	176.56
27.62	10638	179.04
27.89	10762	181.12
28.16	10862	182.81
28.44	10940	184.12
28.71	10998	185.10
28.98	11042	185.83
29.25	11078	186.45
29.52	11118	187.12
29.79	11147	187.60
30.06	11163	187.87

Appendix B. Load Shedding

B.1 Example of CT specimen load shedding procedure

a_{avg} (mm)	a/W	f(a/W)	ΔP (kN)	ΔP (kips)	P_{max} (kips)	P_{min} (kips)	ΔK (MPa \sqrt{m})	K_{max} (MPa \sqrt{m})	K_{min} (MPa \sqrt{m})
10	0.20	4.24	20.24	4.55	5.06	0.51	30	33.33	3.33
10.5	0.21	4.36	19.25	4.33	4.81	0.48	29.375	32.64	3.26
11	0.22	4.49	18.31	4.12	4.57	0.46	28.75	31.94	3.19
11.5	0.23	4.62	17.41	3.91	4.35	0.43	28.125	31.25	3.13
12	0.24	4.75	16.56	3.72	4.14	0.41	27.5	30.56	3.06
12.5	0.25	4.88	15.75	3.54	3.93	0.39	26.875	29.86	2.99
13	0.26	5.01	14.98	3.37	3.74	0.37	26.25	29.17	2.92
13.5	0.27	5.15	14.24	3.20	3.56	0.36	25.625	28.47	2.85
14	0.28	5.28	13.54	3.04	3.38	0.34	25	27.78	2.78
14.5	0.29	5.42	12.86	2.89	3.21	0.32	24.375	27.08	2.71
15	0.30	5.56	12.21	2.75	3.05	0.31	23.75	26.39	2.64
15.5	0.31	5.70	11.59	2.61	2.90	0.29	23.125	25.69	2.57
16	0.32	5.85	11.00	2.47	2.75	0.27	22.5	25.00	2.50
16.5	0.33	6.00	10.42	2.34	2.60	0.26	21.875	24.31	2.43
17	0.34	6.16	9.87	2.22	2.47	0.25	21.25	23.61	2.36
17.5	0.35	6.31	9.34	2.10	2.33	0.23	20.625	22.92	2.29
18	0.36	6.48	8.83	1.99	2.21	0.22	20	22.22	2.22

